International Journal of Earth Sciences (2018) 107:1755–1775
https://doi.org/10.1007/s00531-017-1570-x

ORIGINAL PAPER

The Middle Triassic evolution of the Bangong–Nujiang Tethyan Ocean: evidence from analyses of OIB-type basalts and OIB-derived phonolites in northern Tibet

Jian-Jun Fan[1] · Cai Li[1] · Jin-Heng Liu[1] · Ming Wang[1] · Yi-Ming Liu[1] · Chao-Ming Xie[1]

Received: 12 July 2017 / Accepted: 30 November 2017 / Published online: 18 December 2017

Abstract
In this paper, we present new major and trace element chemical data for the basalts and phonolites of the Nare ocean island fragment (NaOI), as well as zircon U–Pb age data and Hf isotope compositions for the NaOI phonolites in the middle segment of the Bangong–Nujiang Suture Zone, northern Tibet. Our aim is to assess the genesis of these rocks and to reconstruct the Middle Triassic evolution of the Bangong–Nujiang Tethyan Ocean (BNTO). The NaOI retains an ocean island-type double-layered structure comprising a basaltic basement and an oceanic sedimentary cover sequence (conglomerate and limestone, the latter accompanied by layers of erupted phonolite near the top of the sequence). The basalts in the NaOI are enriched in light rare earth elements and high field strength elements (Nb, Ta, Zr, Hf, and Ti), and they exhibit chondrite-normalized REE patterns and primitive mantle-normalized trace element patterns similar to those of ocean island basalts. Taking into consideration their high Dy/Yb, Sm/Yb, and La/Sm ratios, we conclude that the NaOI basalts were derived from the partial melting of garnet peridotite in the mantle. The NaOI phonolites have LREE-enriched chondrite-normalized REE patterns with negative Eu anomalies (Eu/Eu* = 0.41–0.43) and primitive mantle-normalized trace element patterns with enrichments in Nb, Ta, Zr, and Hf, and depletions in Ba, U, Sr, P, and Ti. Given the high contents of Nb (172–256 ppm), Ta (11.8–16.0 ppm), Zr (927–1117 ppm), and Hf (20.8–26.9 ppm), and the very low contents of MgO (0.11–0.25 wt%), the very low $Mg^{\#}$ values (5–10), and the near-zero contents of Cr (1.27–7.59 ppm), Ni (0.43–7.19 ppm), and Co (0.11–0.38 ppm), and the small and homogeneously positive $\varepsilon_{Hf}(t)$ values (+4.9 to +9.5), we infer that the NaOI phonolites were formed by the fractional crystallization of an OIB-derived mafic parent magma. The phonolites of the NaOI contain zircons that yielded U–Pb ages of 239 and 242 Ma, indicating that the NaOI formed during the Middle Triassic. These data, combined with data from modern ocean islands (e.g., Canary Islands, Cape Verde, Fernando de Noronha, Tristan da Cunha, and Gough in the Atlantic Ocean, and Society and Austral–Cook in the Pacific Ocean), lead us to infer that the BNTO was open for a long time before the Middle Triassic, and that the ocean had already developed into a mature ocean with a thick oceanic lithosphere by at least the Middle Triassic.

Keywords Tibetan Plateau · Bangong–Nujiang Tethyan Ocean · Middle Triassic · OIB-type basalts · OIB-derived phonolites

✉ Jian-Jun Fan
fanjj03@163.com

Cai Li
licai010@126.com

Jin-Heng Liu
15948793865@163.com

Ming Wang
wm609@163.com

Yi-Ming Liu
992702229@qq.com

Chao-Ming Xie
xcmxcm1983@126.com

[1] College of Earth Sciences, Jilin University, 2199 Jianshe Street, Changchun 130061, People's Republic of China

Introduction

The Bangong–Nujiang Suture Zone (BNSZ) on the Tibetan Plateau is an important tectonic boundary and metallogenic belt in the eastern section of the Tethys tectonic domain. However, the nature and tectonic evolution of the Bangong–Nujiang Tethyan Ocean (BNTO), represented by the BNSZ, are debated. For example, some scholars have proposed that the BNTO was a long-lived ocean basin that developed continuously from the Paleozoic to the Mesozoic, and that it represents the main basin of the Paleo-Tethys Ocean on the Tibetan Plateau (Pan et al. 1997, 2006, 2012; Wang et al. 2002; Zhu et al. 2013). Others inferred that the BNTO developed mainly during the Mesozoic, opening at first during the Late Permian–Early Triassic, and finally closing during the Cretaceous. In this model, the ocean either represented the northern arm of the Neo-Tethys Ocean (Chang and Zhen 1973; Chang 1978; Smith and Xu 1988; Yin 1997; Ren and Xiao 2004; Shi et al. 2008; Huang et al. 2012; Liu et al. 2014; Fan et al. 2014b, 2015b), or it represented the Meso-Tethys Ocean (Girardeau et al. 1984; Zhou et al. 1997; Wang 2000; Yong and Jia 2000; Wang et al. 2008). Others suggested that the BNTO was a short-lived ocean basin that existed for no more than 100 Myr from the Late Triassic to the Late Jurassic (Kapp et al. 2003, 2007; Qiu et al. 2004; Zhang 2007; Xia et al. 2008; Qu et al. 2010). In this model, it is inferred that the ocean either represented a back-arc ocean basin of the Jinshajiang Paleo-Tethys Ocean or of the Indus–Yarlung Zangbo Neo-Tethys Ocean (Wang et al. 1987). Some scholars have even proposed that the BNTO was not an ocean in the strict sense (Lu et al. 2003; Zhao et al. 2004).

The fundamental problem with the above arguments is that the oldest reliable ages of oceanic BNSZ rocks (e.g., ophiolites and ocean islands) are Late Triassic (Fan et al. 2017) and Early–Middle Jurassic (Qiu et al. 2004; Xia et al. 2008; Shi et al. 2008; Qu et al. 2010; Zhang et al. 2014; Wang et al. 2008, 2013, 2016), and there is a general absence of earlier oceanic remnants, which means little information is available on how and when the early BNTO developed. It is therefore important to find and analyze oceanic remnants of the BNTO in the BNSZ that pre-date the Late Triassic.

In this paper, we describe for the first time the newly discovered Middle Triassic Nare ocean island fragment (NaOI) in the middle segment of the BNSZ (Fig. 1a). We present the results of detailed geochemical, geochronological, and Lu–Hf isotopic analyses of the basalts and phonolites of the NaOI, and we use the data to discuss the genesis and evolution of these rocks. Based on these data and the results of research on modern ocean islands, we also discuss the Middle Triassic evolution of the BNTO.

Geological background and petrological observations

The Tibetan Plateau is located in the eastern section of the Alpine–Himalayan tectonic domain, and is divided from south to north into the Himalayan, Lhasa, Southern Qiangtang, Northern Qiangtang, and Bayan Har–Garze terranes (Fig. 1a; Allègre et al. 1984; Dewey et al. 1988; Pan et al. 1997, 2012; Yin and Harrison 2000; Li et al. 2006; Wang et al. 2013). These terranes are separated by the Indus–Yarlung Zangbo Suture Zone (IYZSZ), the Bangong–Nujiang Suture Zone (BNSZ), the Longmuco–Shuanghu–Lancangjiang Suture Zone (LSLSZ), and the Jinshajiang Suture Zone (JSSZ; Fig. 1a), respectively.

The BNSZ represents the remains of the BNTO and extends eastwards for 2000 km through the areas of Bangong Co, Gerze, Dongqiao, Dingqing, and Jiyuqiao, and into Burma, Thailand, and Malaysia (Fig. 1a; Pan et al. 1997, 2012). The BNSZ in China is divided into three segments, which from west to east are the Bangong Co–Gerze, Gerze–Dingqing, and Dingqing–Nujiang segments (Bureau of Geology and Mineral Exploration of Tibet Province 1993; Pan et al. 1997; Qiu et al. 2004).

The study area is located in the Dong Co region, ~ 90 km to the east of Gerze County in the middle segment of the BNSZ (Fig. 1a). The area contains a number of approximately E–W trending regional structures (Fig. 1b), and the rocks are strongly deformed. The study area contains numerous ophiolites and ocean island fragments, as well as sediments of the Zhanjin, Wuga, Mugagangri, Sewa, Jiebuqu, Langshan, and Jingzhushan groups and formations (Fig. 1b). The Late Carboniferous to Early Permian Zhanjin Formation in this area is dominated by metasandstones and phyllite, whereas the Late Triassic Wuga Formation is dominated by sandstone. The Late Triassic–Jurassic Mugagangri Group consists of deep sea to bathypelagic flysch deposits that formed within the BNTO (Bureau of Geology and Mineral Exploration of Tibet Province 1993; Wang and Zhong 2002; Zeng et al. 2014). The Early–Middle Jurassic Sewa Formation and the Middle Jurassic Jiebuqu Formation are both dominated by shallow marine limestone and sandstone that formed within the BNTO. The Early Cretaceous Langshan Formation consists mainly of limestones that include shallow marine carbonate platform deposits. The newly defined Early Cretaceous Zhaga Formation is dominated by graywacke and shale, and shows load casts, convolute bedding, and a–b–c–d Bouma sequences indicating bathyal to abyssal turbidite deposition (Fan et al. 2015a). The conglomerate- and sandstone-dominated Late Cretaceous Jingzhushan Formation consists of post-collisional molasse that formed within the BNSZ.

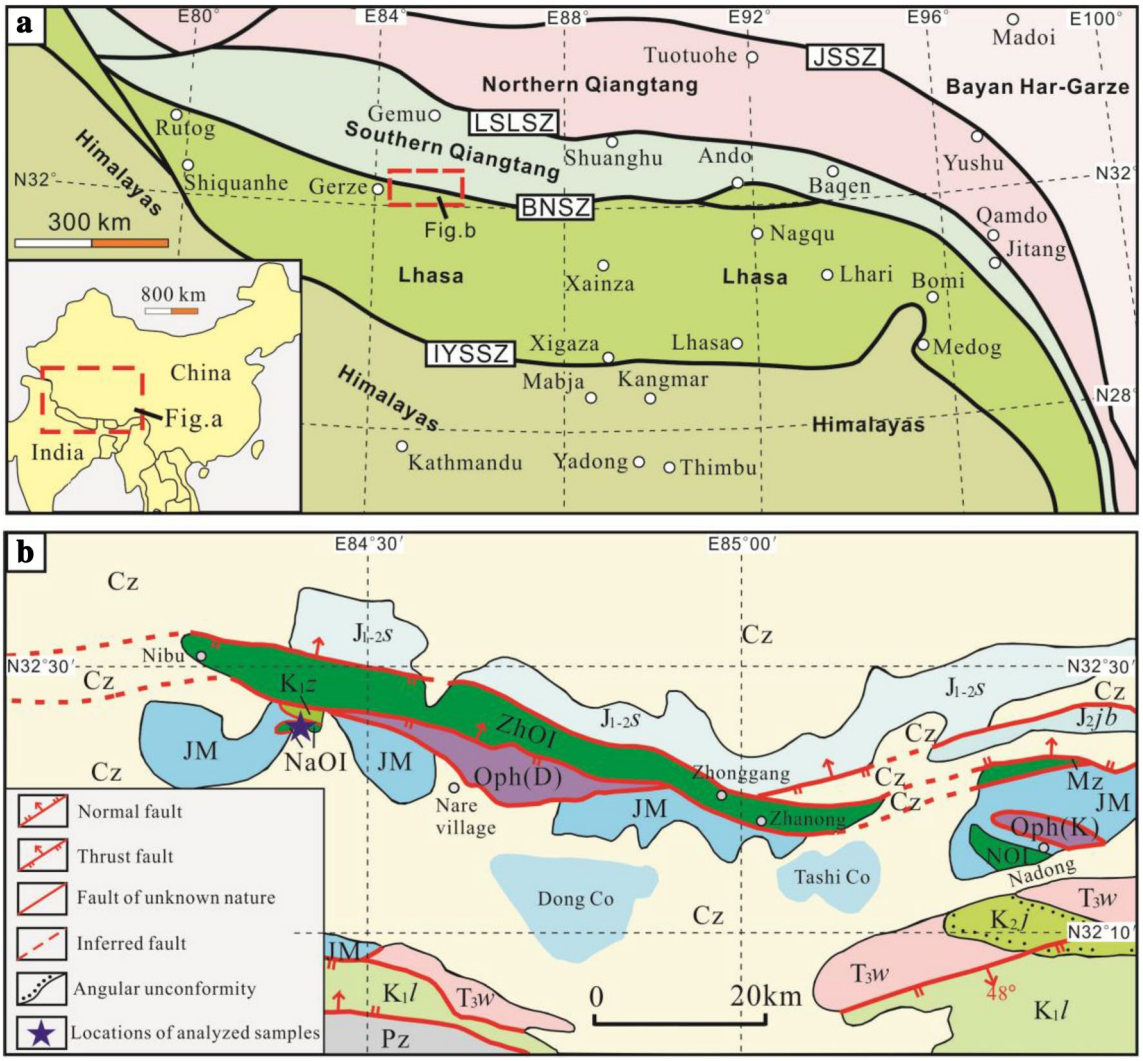

Fig. 1 **a** Tectonic framework of the Tibetan Plateau and **b** geological map of the study area (modified after Fan et al. 2014b). *Cz* Cenozoic, K_2j Late Cretaceous Jingzhushan Formation, K_1l Early Cretaceous Langshan Formation, K_1z Early Cretaceous Zhaga Formation, J_2jb Middle Jurassic Jiebuqu Formation, $J_{1\text{-}2}s$ Early to Middle Jurassic Sewa Formation, *JM* Late Triassic–Jurassic Mugagangri Group, T_3w Late Triassic Wuga Formation, *Pz* late Carboniferous to early Permian Zhanjin Formation, *Oph (D)* Dong Co Ophiolite, *Oph (K)* Kangqiong Ophiolite, *ZhOI* Zhonggang ocean island fragment, *NOI* Nadong ocean island fragment, *NaOI* Nare ocean island fragment

The ophiolites in the study area include the Kangqiong and Dong Co ophiolites. The Kangqiong Ophiolite is located in the eastern part of the study area (Fig. 1b), and is dominated by peridotite, cumulate gabbro, plagiogranite, gabbro, and basalt. A zircon U–Pb age of 115 Ma indicates this ophiolite formed during the Early Cretaceous (Xu et al. 2015). Additional studies have determined that the Kangqiong Ophiolite is a supra-subduction zone (SSZ)-type ophiolite that formed in an extensional fore-arc basin that resulted from intra-oceanic subduction of the Bangong–Nujiang Tethyan oceanic crust during the Early Cretaceous (Xu et al. 2015).

The Dong Co Ophiolite, located in the center of the study area, was emplaced tectonically into the Late Triassic–Jurassic Mugagangri Group and the Jurassic to Early Cretaceous Zhonggang ocean island fragment (Fig. 1b). The Dong Co Ophiolite represents a section of oceanic crust that is more than 5 km thick and consists of ultramafic rocks, serpentinite, troctolite, gabbro (either massive or exhibiting cumulate textures), and a sheeted dike complex of diabase, pillow basalt, plagiogranite, and minor radiolarian chert (Qiu et al. 2004; Bao et al. 2007; Zhang 2007; Zeng et al. 2010; Li et al. 2013; Wang et al. 2016). In addition, the Dong Co Ophiolite contains the dunite–troctolite–olivine gabbro (DTG) series of rocks (Bao et al. 2007), as well as minor amphibolite facies metamorphic rocks (Wang et al. 2008).

The interpretation that the Dong Co Ophiolite formed during the Jurassic was based mainly on the following two lines of evidence: (1) an Early Jurassic Sm–Nb isotopic age of 191 ± 22 Ma was obtained from the cumulate gabbro of the Dong Co Ophiolite, and Late Jurassic to Early Cretaceous K–Ar ages of 140 ± 4.07 and 152.30 ± 3.60 Ma were obtained from the same cumulate gabbro samples (Qiu et al. 2004); and (2) some Jurassic radiolarians occur in chert in the Dong Co area surrounding the Dong Co Ophiolite (Zeng et al. 2010). However, Bao et al. (2007) recently obtained Early Cretaceous ages of 132 Ma (SHRIMP U–Pb zircon) from the cumulate gabbro, and 137 Ma (whole rock ^{40}Ar–^{39}Ar) and 141 Ma (whole rock ^{40}Ar–^{39}Ar) from the basalt of the Dong Co Ophiolite, indicating that the Dong Co Ophiolite formed during the Early Cretaceous (Bao et al. 2007). In addition, Wang et al. (2016) obtained a Middle Jurassic age of 164 Ma (LA–ICP–MS zircon U–Pb) from the cumulate gabbro (Wang et al. 2016). Given that geochronological studies of the Dong Co Ophiolite have reported Jurassic and Cretaceous ages, we propose that the Dong Co Ophiolite represents a multi-stage tectonic mélange that formed during the Jurassic to Early Cretaceous.

The ocean island fragments in the study area include Zhonggang, Nadong, and Nare (Fig. 1b), and these different fragments represent different ocean islands that formed in the BNTO with different ages. The Zhonggang ocean island fragment is the largest ocean island fragment in the BNSZ, covering an area of > 400 km^2 (Zeng et al. 2010; Fan et al. 2014b). Similar to modern ocean islands, the Zhonggang ocean island fragment has a double-layered lithological structure with a mafic basement of basalt and gabbro and an oceanic sedimentary cover sequence of limestone, chert, and conglomerate (Fan et al. 2014b). Early Jurassic and Early Cretaceous U–Pb zircon and $^{40}Ar/^{39}Ar$ ages indicate the Zhonggang ocean island fragment formed from a long-lived hotspot that was active from the Early Jurassic to the Early Cretaceous (Zeng et al. 2010; Zhang et al. 2014; Fan et al. 2014b, 2015b), and these age data supported that the BNTO was still at least partially open, and developing during the Early Cretaceous. The Nadong ocean island fragment covers an area of > 50 km^2, has an E–W extent of > 25 km, and is dominated by basalt, gabbro, limestone, and conglomerate. Jurassic fossils and U–Pb zircon ages have been obtained from this ocean island fragment, indicating formation in the Jurassic (Fan et al. 2014a). The existence of the Jurassic Nadong ocean island fragment indicates that the BNTO was ongoing during this time.

The Nare ocean island fragment (NaOI) covers an area of > 5 km^2 (Fig. 1b). Similar to the Zhonggang and Nadong ocean island fragments, the NaOI has a double-layered lithological structure with a basaltic basement and an oceanic sedimentary cover sequence of limestone and conglomerate with eruptive phonolite at the top of the sequence. Three stages in the evolution of NaOI have been identified: (1) formation of the basaltic basement, (2) deposition of the oceanic sedimentary cover sequence (basaltic conglomerate and limestone), and (3) the eruption of layers of evolved phonolitic magma within the upper part of the sedimentary sequence (Fig. 2). It was initially thought that the contact between the NaOI and the Zhaga Formation was conformable (Fan et al. 2015a), but detailed research as part of the present study has shown a fault contact (Fig. 1b), as indicated by the existence of tectonic deformation (Fig. 3a), tectonic breccias (Fig. 3b), and fault springs along the contact of the NaOI and the Zhaga Formation.

The basalts within the NaOI are generally gray–green in color (Fig. 3c), and are present as individual units that generally have thicknesses of > 10 m (Fig. 2). The basalts are aphanitic with an intergranular matrix (Fig. 3d). The basalts contain numerous amygdales (up to 30%) of calcite (Fig. 3d). The basaltic conglomerates within the NaOI contain gravel clasts and matrix, both of which are made up of basaltic debris (Fig. 2), and it is noteworthy that the basaltic conglomerates contain no terrestrial debris. The conglomerates provide evidence of a sedimentary environment with a restricted provenance, proximal deposition in a far-shore type setting, and rapid accumulation in the ocean that surrounded the island. The limestones within the NaOI form thick layers that lack terrestrial debris (Fig. 2), and they record deposition in an isolated, clear water sedimentary environment associated with a carbonate platform. The phonolites, which occur as layers within the upper part of the sequence of NaOI cover sediments (Fig. 2), are present as individual units that have total thicknesses of > 30 m. The phonolites are generally gray–white in color (Fig. 3e), and are aphanitic with an interwoven matrix consisting of abundant alkali feldspar with interstitial plagioclase, feldspathoids, and rare mafic minerals (Fig. 3f).

Analytical methods

Whole–rock major and trace element analyses

Five NaOI basalt samples and fifteen NaOI phonolite samples were collected for whole-rock major and trace element analyses. Samples were trimmed to remove weathered surfaces, cleaned with deionized water, crushed, and powdered in an agate mill. Major element compositions were analyzed by inductively coupled plasma–optical emission spectroscopy (ICP–OES; Leeman Prodigy) with high-dispersion Echelle optics at the China University of Geosciences, Beijing, China. Loss on ignition (LOI) values were determined by heating 1 g of sample in a furnace at 1000 °C for several hours before being cooled in a desiccator and reweighed. Analytical uncertainties for the major elements

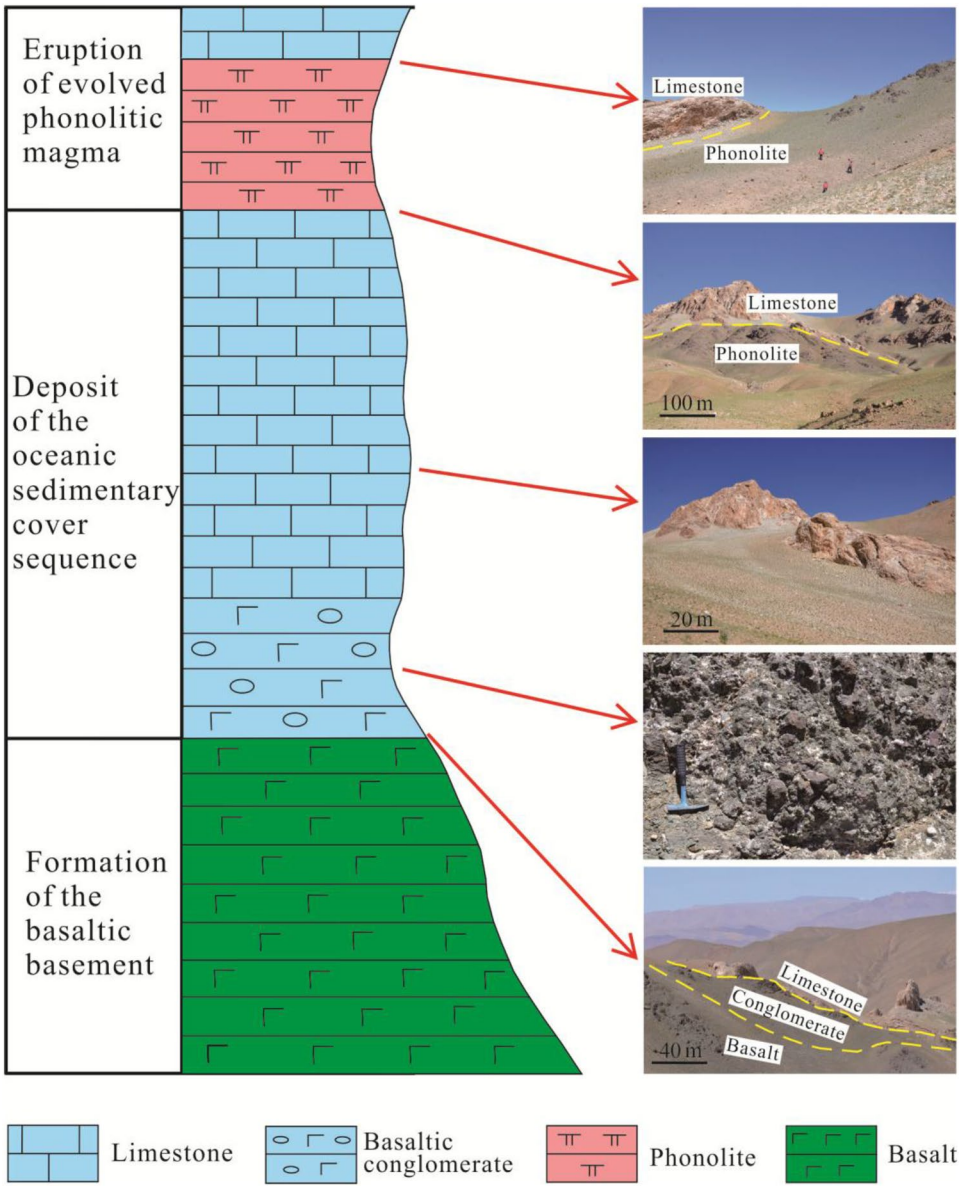

Fig. 2 Stratigraphic column for the Nare ocean island fragment

are generally < 1 wt%. Trace element compositions were analyzed by inductively coupled plasma–mass spectrometry (ICP-MS; Agilent-7500a) at the China University of Geosciences, Beijing, China. Analytical accuracy and precision during trace element analysis were calculated from analyses of two standards: AGV-2 (US Geological Survey standard) and GSR-3 (Chinese national geological reference standard). Analytical accuracy, calculated from the relative difference between measured and recommended values, is < 5 wt% for most elements. Analyses of the AGV-2 and GSR-3 international standards are in good agreement with recommended values (Govindaraju 1994). For details on the analytical procedures, see Zhai et al. (2013).

In situ zircon U–Pb LA–ICP–MS analysis

Two samples from the NaOI phonolite were selected for in situ zircon U–Pb analyses. The zircons were separated by conventional heavy liquid and magnetic techniques at the Special Laboratory of the Geological Team of Hebei Province, Langfang, China. The internal structures of zircon were characterized under cathodoluminescence (CL) at the Institute of Physics, Peking University, Beijing, China to select analytical points for laser ablation–inductively coupled plasma–mass spectroscopy (LA–ICP–MS) analyses. U, Th, and Pb isotopes and trace element zircon analyses were carried out by LA–ICP–MS at the Geological Laboratory Centre, China University of Geosciences, Beijing, China. The spot size was 36 and 25 μm for each sample. Helium

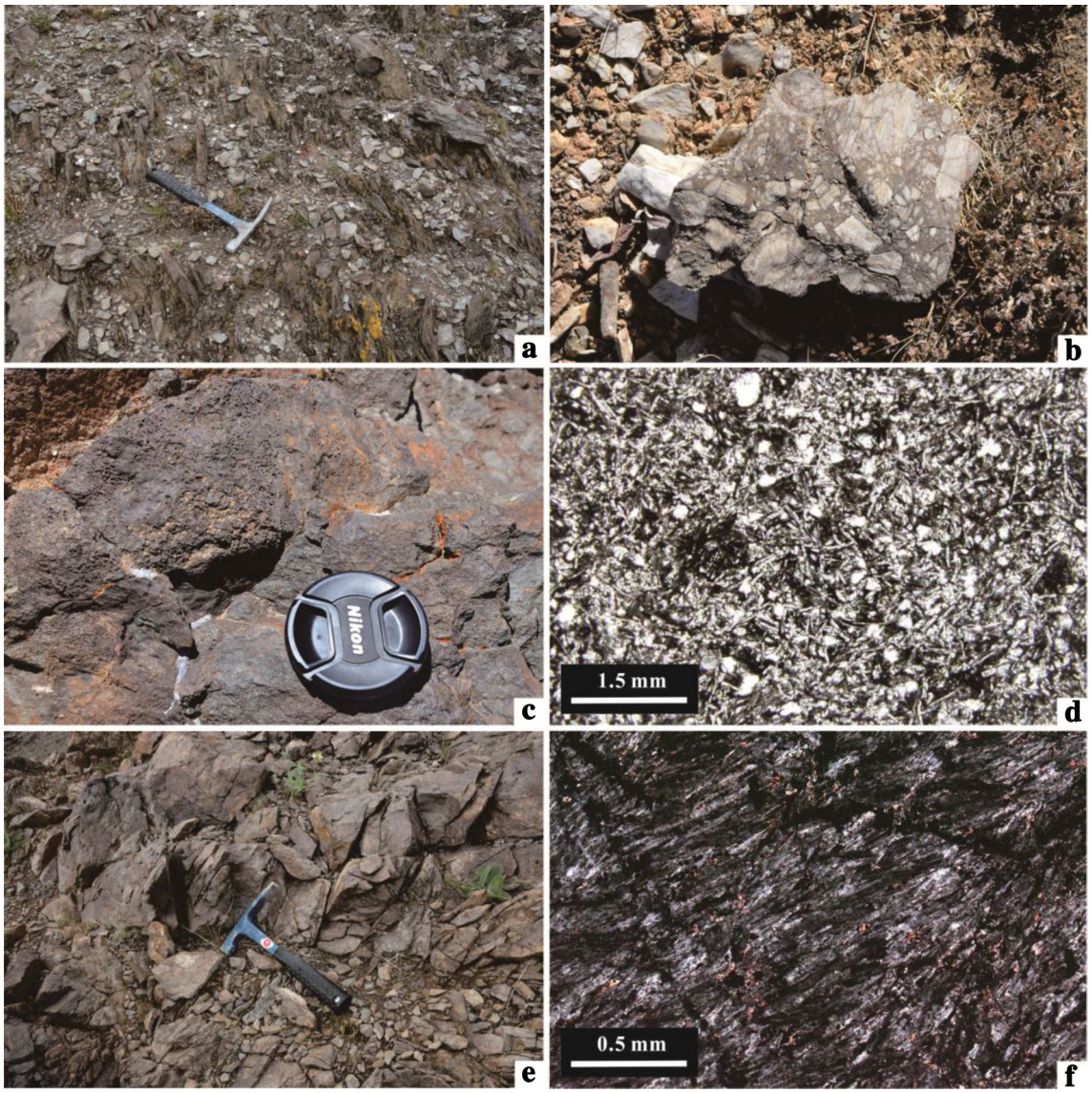

Fig. 3 **a** Photograph of tectonic deformation within the Zhaga Formation along the contact of the NaOI and the Zhaga Formation. **b** Photograph of tectonic breccia within the NaOI along the contact of the NaOI and the Zhaga Formation. **c** Photograph of NaOI basalt. **d** Photomicrograph of NaOI basalt. **e** Photograph of NaOI phonolite. **f** Photomicrograph of NaOI phonolite

was used as a carrier gas. Reference and internal zircon standards 91500 (Wiedenbeck et al. 1995) and NIST610 (29Si), respectively, were used for instrument calibration. The Pb correction method of Anderson (2002) was applied. For further details of the analytical techniques, see Yuan et al. (2004). Reported uncertainties for the age analyses are given as 1σ values with weighted mean ages in the 95% confidence level. Isotopic data were processed using the GLITTER (version 4.4) and Isoplot/Ex (version 3.0) programs (Ludwig 2003).

In situ zircon Hf isotope analyses

In situ zircon Hf isotope analyses were performed on 17 previously dated zircon grains from the NaOI phonolite samples. The points used for the Hf analyses were the same as those used during the LA–ICP–MS analyses, which were selected from CL images. The data were collected using a NEPTUNE Plus MC–ICP–MS at the Beijing Createch Testing Technology Co., Ltd, Beijing. A single spot ablation mode with a spot size of 55 μm was used to acquire the data. Each measurement consisted of 20 s of background signal acquisition followed by 50 s of ablation signal acquisition. Detailed information on the

operating conditions and analytical methods can be found in Hu et al. (2012). The analyzed $^{176}Hf/^{177}Hf$ ratios for the zircon standard (91500) were 0.282299 ± 31 ($2\sigma_n$, n-40), which are similar to the $^{176}Hf/^{177}Hf$ ratios of 0.282302 ± 8 and 0.282306 ± 8 (2σ) for the standard when determined by the solution method (Goolaerts et al. 2004; Woodhead et al. 2004). Off-line selection, integration of analyte signals, and mass bias calibrations were performed using the ICP–MS DataCal program (Liu et al. 2010).

Results

Whole-rock major and trace element geochemistry

NaOI basalts

Whole-rock major and trace element data for the NaOI basalts are given in Table 1. The NaOI basalts have undergone varying degrees of carbonate alteration (Fig. 3d), resulting in variable values of LOI and changes in the concentrations of mobile elements (e.g., Na, K, Ca, Cs, Rb, Ba, and Sr) compared with protolith values. However, concentrations and ratios of immobile elements (e.g., REE, Nb, Ta, Zr, Hf, Ti, and P) and transition metal elements (e.g., V, Ni, Cr, and Fe) have not been affected by these processes, and can therefore be used to investigate the petrogenesis and tectonic setting of the samples.

The five basalt samples have variable contents of SiO_2 (45.1–52.1 wt%), high contents of TiO_2 (2.90–3.31 wt%), Fe_2O_3 (9.14–11.5 wt%), MgO (4.41–7.47 wt%), CaO (7.61–12.1 wt%), and Na_2O (3.09–3.76 wt%), low contents of K_2O (1.23–1.85 wt%), and low $Mg^{\#}$ values (53–61). The NaOI basalts have much higher TiO_2 contents (2.90–3.31 wt%) than typical island-arc volcanic rocks (0.58–0.85 wt%) and mid-ocean ridge basalts (MORB; 1.0–1.5 wt%), but similar contents to those of OIB (2.20 wt%; Hishashi 1954; Irvine and Baragar 1971; Winchester and Flody 1977; Pearce 1983).

The samples of NaOI basalt have high total REE concentrations (147–180 ppm), and they exhibit light rare earth element (LREE)-enriched chondrite-normalized REE patterns (La_N/Yb_N = 8.80–10.4; Fig. 4a; Sun and McDough 1989). These samples are enriched in high field strength elements (HFSEs; Nb, Ta, Zr, Hf, and Ti) and exhibit primitive mantle-normalized trace element patterns similar to those of OIB (Fig. 4b; Sun and McDough 1989).

All the NaOI basalt samples fall in the field of alkali basalt on a Zr/TiO_2*0.0001 vs. Nb/Y immobile element classification diagram (Fig. 5a; Winchester and Flody 1977), and these samples plot in the intraplate basalt

Table 1 Major (wt%) and trace element (ppm) data for the basalt in the Nare Ocean Island

Sample	NH1	NH2	NH3	NH4	NH5
SiO_2	45.1	47.5	51.2	50.6	52.1
TiO_2	3.31	3.05	2.90	3.25	2.93
Al_2O_3	12.1	12.5	10.4	10.9	10.3
Fe_2O_3	11.5	11.4	9.14	10.5	11.1
MnO	0.15	0.16	0.13	0.13	0.15
MgO	5.63	7.47	4.41	5.12	5.51
CaO	12.1	7.61	11.5	8.45	8.06
Na_2O	3.09	3.59	3.44	3.76	3.34
K_2O	1.85	1.14	1.23	1.31	1.32
P_2O_5	0.47	0.44	0.36	0.37	0.33
LOI	3.32	4.02	4.66	5.06	4.29
Sc	26.4	28.9	24.5	27.4	26.4
V	300	323	291	332	307
Cr	235	234	178	197	240
Co	45.6	45.1	42.4	40.9	39.4
Ni	111	101	84.5	74.4	85.1
Cu	98.7	103	91.3	105	90.8
Ga	20.7	21.2	18.3	20.5	20.6
Rb	36.9	23.3	24.0	27.1	24.3
Sr	223	180	223	200	161
Y	27.2	27.6	24.6	28.7	25.5
Zr	218	234	204	240	209
Nb	33.9	23.9	40.8	48.0	42.1
Cs	0.73	0.73	0.40	1.03	0.79
Ba	231	738	192	191	347
La	26.3	28.9	24.1	31.4	23.0
Ce	62.5	65.7	54.3	67.7	53.4
Pr	8.01	8.36	6.95	8.46	6.91
Nd	35.1	36.6	31.7	37.9	31.6
Sm	8.21	8.49	7.36	8.57	7.49
Eu	2.67	2.87	2.41	2.81	2.45
Gd	8.11	8.43	7.37	8.54	7.43
Tb	1.14	1.18	1.00	1.17	1.03
Dy	6.24	6.50	5.60	6.51	5.74
Ho	1.10	1.14	0.96	1.12	0.99
Er	2.80	2.94	2.49	2.92	2.55
Tm	0.35	0.36	0.30	0.36	0.31
Yb	2.05	2.19	1.84	2.16	1.88
Lu	0.27	0.29	0.24	0.28	0.25
Hf	5.27	5.63	5.24	6.10	5.31
Ta	2.68	1.35	2.50	2.96	2.59
Pb	2.28	3.32	1.76	2.20	1.97
Th	3.27	3.42	2.89	3.39	2.88
U	0.87	1.09	0.60	1.04	0.63

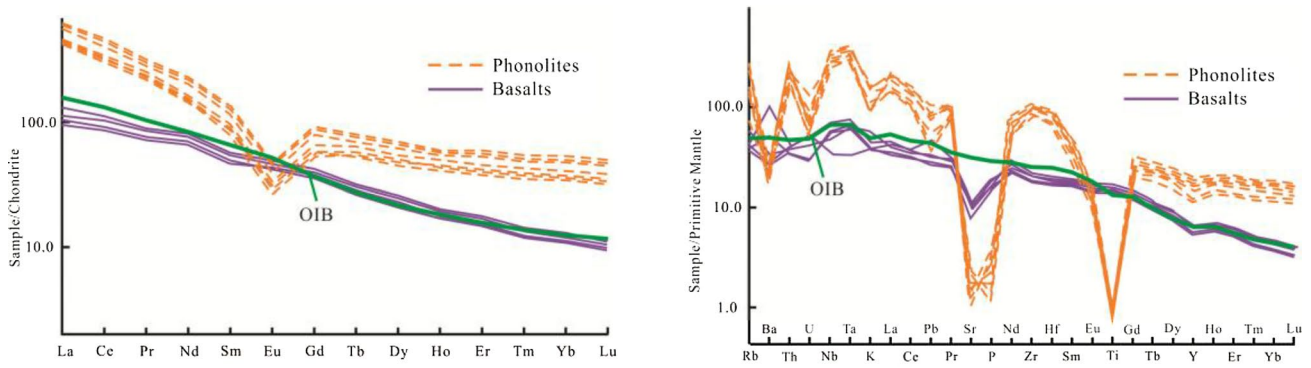

Fig. 4 **a** Chondrite-normalized REE variation diagram for samples of NaOI basalt and phonolite. **b** Primitive mantle-normalized trace element variation diagram for samples of NaOI basalt and phonolite

(ocean island basalt) fields on the V vs. Ti/1000 diagram (Fig. 5b), the Ti/100 vs. Zr vs. (Y × 3) diagram (Fig. 5c; Pearce and Cann 1973), and the (2 × Nb) vs. Zr/4 vs. Y diagram (Fig. 5d; Meschede 1986), indicating they formed from OIB-type magma.

NaOI phonolites

Whole-rock major and trace element data for the NaOI phonolites are given in Table 2. Although the NaOI basalts have undergone varying degrees of carbonate alteration, very limited alteration has occurred within the NaOI phonolites, as indicated by the field and petrographic observations (Fig. 3e, f), and supported by the very low LOI values (0.90–1.91 wt%) and the consistent primitive mantle-normalized multi-element variation diagram patterns, including the LILE patterns of these samples. Mobile elements (e.g., Na, K, Ca, Cs, Rb, Ba, and Sr) can therefore be used to investigate the petrogenesis and tectonic setting of the samples.

Fifteen samples of the NaOI phonolite have high contents of SiO_2 (60.3–65.3 wt%), Al_2O_3 (16.8–19.3 wt%), Na_2O (6.12–8.27 wt%), K_2O (2.85–5.19 wt%), and Fe_2O_3 (4.51–5.37 wt%), low contents of TiO_2 (0.15–0.20 wt%) and MgO (0.11–0.25 wt%), and very low $Mg^{\#}$ values (5–10). Similar to the samples of the NaOI basalt, the samples of the NaOI phonolite have high total REE concentrations (430–619 ppm), and they exhibit LREE-enriched chondrite-normalized REE patterns (La_N/Yb_N = 10.8–13.3) with negative Eu anomalies (Fig. 4a; Eu/Eu* = 0.41–0.43; Sun and McDough 1989). The NaOI phonolites are enriched in Nb, Ta, Zr, and Hf, and depleted in Ba, U, K, Sr, P, and Ti in the primitive mantle-normalized trace element patterns (Fig. 4b; Sun and McDough 1989). In addition, all the NaOI phonolite samples fall in the phonolite field on a Zr/TiO_2*0.0001 vs. Nb/Y immobile element classification diagram (Fig. 5a; Winchester and Flody 1977).

Zircon U–Pb ages

LA–ICP–MS U–Pb data for the zircons in the NaOI phonolites are given in Tables 3 and 4. The zircons are generally hypidiomorphic short prisms (50–200 μm long) with aspect ratios of 1:1 to 2:1. They are typically gray, and exhibit widely magmatic oscillatory zoning in CL images (Fig. 6). Zircon grains from the phonolites of NaOI have ΣREE contents of 448–8104 ppm, with an average of 3099 ppm. All the zircons display fractionated rare earth element (REE) patterns, heavy REE (HREE) enrichment and light REE (HREE) depletion, and clear negative Eu and variable positive Ce anomalies (Fig. 6). Their Th/U ratios are 0.27–2.67, with an average of 1.30. All the above features indicate that the zircons are of magmatic origin (Hoskin and Black 2000). The zircons from the phonolites yielded Middle Triassic weighted mean $^{206}Pb/^{238}U$ ages of 238.8 ± 2.8 Ma (MSWD = 3.30) and 241.9 ± 1.9 Ma (MSWD = 1.90) (Fig. 6).

Because the phonolites occur as layers within the upper part of the sequence of NaOI cover sediments (Fig. 2), the Middle Triassic ages of the NaOI phonolites (239–242 Ma) should represent the age of formation of the NaOI. Therefore, we conclude that the NaOI and the NaOI phonolite formed during the Middle Triassic.

Zircon Lu–Hf isotope data

Some of the analytical spots for U–Pb dating of zircons from the NaOI phonolites were also used for in situ Hf isotope analysis (Fig. 6), and zircon Lu–Hf isotope data for the NaOI phonolites are given in Table 5. The initial $^{176}Hf/^{177}Hf$ ratios for primary zircons of the NaOI phonolites with ages of ~239 Ma vary from 0.282763 to 0.282893, yielding $\varepsilon_{Hf}(t)$ values and T^{C}_{DM} model ages (T_{DM1}) of +4.9 to +9.5 and 522 to 716 Ma, respectively. The initial $^{176}Hf/^{177}Hf$ ratios

for primary zircons of the NaOI phonolites with ages of ~242 Ma vary from 0.282773 to 0.282886, yielding $\varepsilon_{Hf}(t)$ values and T^{C}_{DM} model ages (T_{DM1}) of +5.4 to +9.4 and 567–693 Ma, respectively. These values indicate that the NaOI phonolites were derived from the partial melting of juvenile crust or by fractional crystallization of the mantle-derived mafic parental magma.

Discussion

Petrogenesis of the NaOI basalts and phonolites

Crustal contamination

Before discussing the magma source of the analyzed basalts and phonolites, it is necessary to consider whether they record any crustal contamination. Th and Ta are sensitive indicators of crustal contamination, as contamination results in a marked increase in Th/Ta ratios (Condie 1993). All the NaOI basalts and phonolites have relatively low Th/Ta ratios (1.11–2.54, and 0.93–1.53, respectively), similar to those in volcanic rocks derived from primitive mantle (Th/Ta = 2.3; Condie 1993) and much lower than those of the upper crust (Th/Ta > 10), indicating that none of these phonolites or basalts record crustal contamination. In addition, the NaOI basalts and phonolites have high contents of Nb (23.9–48.0 and 172–256 ppm, respectively) and Ta (1.35–2.96 and 11.8–16.0 ppm, respectively). Furthermore, these rocks do not show Pb enrichment in primitive mantle-normalized trace element patterns (Fig. 4b), further excluding the possibility that they underwent significant crustal contamination, because continental crust (CC) is characterized by depletions in Nb and Ta, and significant enrichment in Pb (Rudnick and Gao 2003; Niu 2009). If the NaOI basalts and phonolites had undergone crustal contamination, a CC signature would have been apparent in the elemental data, but no such signature exists.

Magma source

Various studies have shown that basaltic magmas are commonly derived from the partial melting of mantle peridotite, and that their REE patterns are controlled mainly by the contents of garnet and spinel in their magma source rather than by the contents of olivine, clinopyroxene, or orthopyroxene, or by pressure and temperature (McKenzie and O'Nions 1991; Beattie 1994; Horn et al. 1994; Schwandt and McKay 1998). In general, basalts derived from spinel lherzolite have flat chondrite-normalized REE patterns with inconspicuous fractionation between the LREEs and the heavy REEs (HREEs). However, basalts derived from garnet lherzolite display obvious fractionation between the LREEs and HREEs, and high La_N/Yb_N and Ce_N/Yb_N ratios (Hart and Dunn 1993; Hauri et al. 1994). In addition, partial melting of a spinel lherzolite mantle source does not change the Sm/Yb ratio because both Sm and Yb have similar partition coefficients, whereas it may decrease La/Sm ratios and Sm contents of the melts (Aldanmaz et al. 2000). Therefore, partial melts of a spinel lherzolite source should define melting trends sub-parallel to and nearly coincident with, a mantle array defined by depleted to enriched source compositions (Fig. 7a). On the other hand, garnet has a high partition coefficient for Yb ($D_{garnet/melt} = 6.6$) relative to Sm ($D_{garnet/melt} = 0.25$) (Johnson 1994), so that partial melting of garnet lherzolite mantle with residual garnet will produce a more steeply sloping trend on a Sm/Yb vs. La/Sm diagram than will melting of spinel lherzolite (Fig. 7a).

The NaOI basalts have LREE-enriched chondrite-normalized REE patterns ($La_N/Yb_N = 8.80–10.4$; Fig. 4), similar to the patterns of basalts derived from garnet peridotite. That garnet peridotite in the mantle was the magma source of the NaOI basalts, is further supported by (1) the high Dy/Yb (2.96–3.06), Sm/Yb (3.87–4.00), and La/Sm (3.07–3.41) ratios of these basalts; and (2) the fact that the NaOI basalts plot in an area on the Sm/Yb vs. La/Sm diagram that corresponds to 5–10% partial melting of garnet peridotite (Fig. 7a; Sun and McDonough 1989; McKenzie and O'Nions 1991; Aldanmaz et al. 2000; Zhao and Zhou 2007).

Phonolites are volcanic rock types characteristic for intraplate settings at oceanic and continental environments (Ackerman et al. 2015), and two possible hypotheses have been proposed for their genesis: (1) fractional crystallization of mafic parental melts and (2) combined assimilation–fractional crystallization process involving a substantial crustal contamination during the ascent (Barberi et al. 1975; Baker and McBirney 1985; Vieten et al. 1988; Macciotta et al. 1990; Enders et al. 1992; Jung et al. 2013; Ackerman et al. 2015).

In the case of the NaOI phonolites, they have not underwent any crustal contamination, as discussed in Sect. 6.1.1, and this exclude the possibility that they formed at continental environments by the second genesis hypotheses. The inference is further supported by the small and homogeneously positive $\varepsilon_{Hf}(t)$ values of the NaOI phonolites (+4.9 to +9.5). If the NaOI phonolites formed at continental environments by the second genesis hypotheses that combined assimilation–fractional crystallization process involving a substantial crustal contamination during the ascent, the $\varepsilon_{Hf}(t)$ values would be various and mostly negative. We infer, therefore, that the NaOI phonolites were formed by fractional crystallization of a mafic parental magma. The very low contents of MgO (0.11–0.25 wt%), the very low $Mg^{\#}$ values (5–10), and the near-zero contents of Cr (1.27–7.59 ppm), Ni (0.43–7.19 ppm), and Co (0.11–0.38 ppm) indicate that the phonolites underwent substantial fractional crystallization,

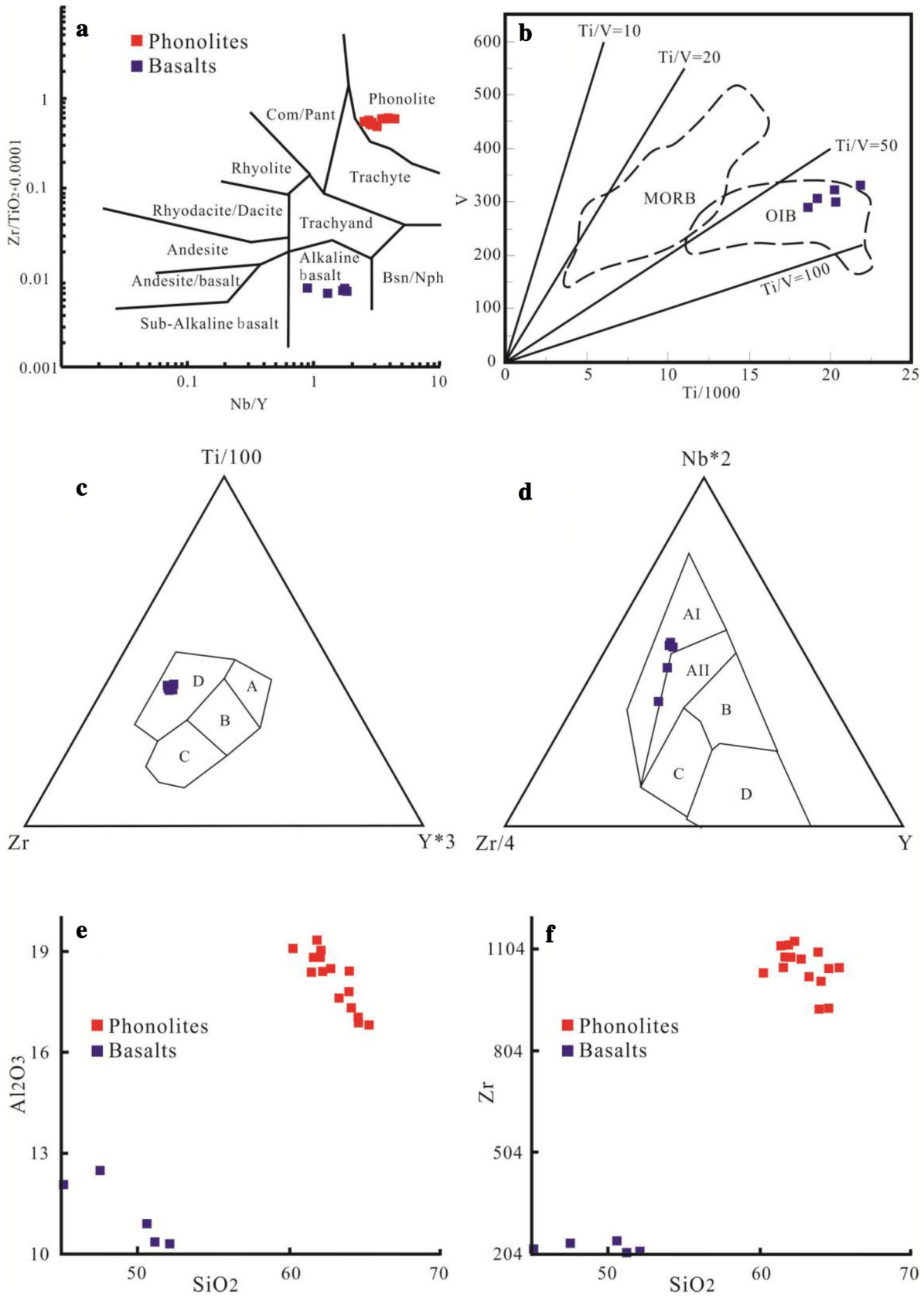
a
Phonolites
Basalts
Phonolite
Com/Pant
Rhyolite
Trachyte
Rhyodacite/Dacite
Trachyand
Andesite
Alkaline basalt
Andesite/basalt
Bsn/Nph
Sub-Alkaline basalt
Zr/TiO2*0.0001
Nb/Y
b
Ti/V=10
Ti/V=20
Ti/V=50
Ti/V=100
MORB
OIB
V
Ti/1000
c
Ti/100
D
A
B
C
Zr
Y*3
d
Nb*2
AI
AII
B
C
D
Zr/4
Y
e
Phonolites
Basalts
Al2O3
SiO2
f
Phonolites
Basalts
Zr
SiO2

◂**Fig. 5** **a** Immobile element-based classification diagram showing the nature of the basalts and phonolites analyzed during this study. **b** NaOI basalts plotted on the V vs. Ti/100 diagram. **c** NaOI basalts plotted on the Ti/100 vs. Zr vs. Y × 3 diagram (*A* island-arc tholeiite, *B* mid-ocean ridge basalt (MORB) + island-arc tholeiite and calc-alkali basalt, *C* calc-alkaline basalt, *D* intraplate basalt). **d** NaOI basalts plotted on the 2 × Nb vs. Zr/4 vs. Y diagram (*AI* intraplate alkali basalt, *AII* intraplate alkali basalt and tholeiite, *B* E-type MORB, *C* intraplate tholeiite and volcanic arc basalt, *D* N-type MORB and volcanic arc basalt). **e** Al_2O_3 vs. SiO_2 diagram. **f** Zr vs. SiO_2 diagram

which in turn is consistent with the inference that they were formed by fractional crystallization of a mafic parental magma. In addition, the NaOI phonolites are enriched in LREE and high-field strength elements (Nb, Ta, Zr, and Hf), and they exhibit chondrite-normalized REE patterns and primitive mantle-normalized trace element patterns that are similar to those of OIB-derived magmas (Fig. 4a, b). We infer, therefore, that the NaOI phonolites were formed by fractional crystallization of an OIB-derived mafic parental magma. However, the absence of a negative correlation on some Harker diagrams (e.g., Al_2O_3–SiO_2 and Zr–SiO_2 diagrams; Fig. 5e, f) within the NaOI basalts and phonolites indicate that the NaOI phonolites could not have been produced by fractional crystallization of the basalts analyzed in this paper, and that there are some another associated OIB-type mafic parental magma existed within the primitive Nare Ocean Island.

Fractional crystallization

The Cr and Ni concentrations in the NaOI basalts, as well as their $Mg^{\#}$ values (Cr = 178–240 ppm, Ni = 74.4–111 ppm, $Mg^{\#}$ = 53–61), are generally lower than the values for primary-mantle-derived magmas (Cr = 300–500 ppm, Ni = 300–400 ppm, $Mg^{\#}$ = 68–76; Frey et al. 1978; Hess 1992). This indicates that the NaOI basaltic magmas underwent fractional crystallization of olivine, chromite, and pyroxene.

Fractional crystallization of the NaOI basaltic magma is also evident in variation diagrams of Fe_2O_3–MgO, TiO_2–MgO, P_2O_5–MgO, Cr–MgO, and Ni–MgO (Fig. 7b–f). The existence of negative correlations between Fe_2O_3 and MgO (Fig. 7b) and TiO_2 and MgO (Fig. 7c) indicates the fractionation of Fe–Ti oxides (e.g., ilmenite and rutile), and the existence of a negative correlation between P_2O_5 and MgO (Fig. 7d) indicates the fractionation of apatite. The Cr contents of the NaOI basalts decrease with decreasing MgO content (Fig. 7e), indicating fractional crystallization of olivine. The Ni contents of the NaOI basalts also decrease with decreasing MgO content (Fig. 7f), indicating fractional crystallization of pyroxene. The absence of negative Eu anomalies in the chondrite-normalized REE patterns (Fig. 4a) indicates the limited fractionation of plagioclase.

As stated above, the NaOI phonolites underwent substantial fractional crystallization. The negative Eu anomalies (Fig. 4a; Eu/Eu* = 0.41–0.43) in the chondrite-normalized REE patterns indicate the fractionation of plagioclase. The remarkable negative anomalies in P and Ti in the primitive mantle-normalized trace element patterns (Fig. 4b) resulted from the extraction of P- and Ti-rich phases such as apatite, Fe–Ti oxides, and other Ti-bearing minerals. The negative Ba and K anomalies in the primitive mantle-normalized trace element patterns (Fig. 4b) indicate the fractionation of feldspar, whereas the negative U anomalies (Fig. 4b) were probably generated by fractional crystallization involving fractionated mineral assemblages with high uranium partition coefficients, such as titanomagnetite, titanite, and apatite.

In summary, the NaOI basalts were derived from the partial melting of garnet peridotite in the mantle. The ascending magmas underwent varying degrees of fractional crystallization but were not contaminated by the crust. The NaOI phonolites were formed by fractional crystallization of the OIB-type mafic parental magma. Similar to the NaOI basalts, the ascending magmas of the NaOI phonolites were not contaminated by the crust.

Tectonic setting: implications for the Middle Triassic evolution of the Bangong–Nujiang Tethyan Ocean

The NaOI retains an ocean island-type double-layered structure with a basaltic basement and an oceanic sedimentary cover sequence (conglomerate and limestone, the latter accompanied by layers of erupted phonolite near the top of the sequence), similar to the ocean island in the modern ocean (e.g., the Brava Ocean Island in the Atlantic Ocean; Mourão et al. 2010). Geochemical and Hf isotopic analyses of the NaOI basalts and phonolites show that the NaOI basalts are OIB-type volcanic rocks, and that the NaOI phonolites were formed by fractional crystallization of the OIB-type mafic parental magma. Neither the OIB-type nor the OIB-derived magma underwent crustal contamination during ascent. All the petrological and geochemical features described in this paper demonstrate that the NaOI was a typical ocean island that formed in the BNTO.

Phonolite is a relatively rare rock type in nature, and it makes up only one thousandth of the volume of extrusive volcanic rocks. Phonolite is also rare in modern ocean islands, as it was indicated by that although there are tens of thousands of modern ocean islands, very few have been reported to contain phonolite. For this study, we undertook a survey of modern ocean islands to record those that contain phonolite. Excluding ocean islands that have a controversial genesis (e.g., the Kerguelen archipelago in the Indian

Table 2 Major (wt%) and trace element (ppm) data for the phonolite in the Nare Ocean Island

Sample	NH6	NH7	NH8	NH9	NH10	NH11	NH12	NH13	NH14	NH15	NH16	NH17	NH18	NH19	NH20
SiO_2	62.8	60.3	62.1	64.0	61.8	62.3	61.6	62.1	61.5	65.3	64.6	63.3	64.1	63.9	64.6
TiO_2	0.18	0.20	0.19	0.18	0.20	0.19	0.20	0.19	0.19	0.17	0.15	0.16	0.16	0.17	0.17
Al_2O_3	18.5	19.1	19.0	18.4	19.3	18.4	18.8	18.8	18.4	16.8	16.9	17.6	17.3	17.8	17.0
Fe_2O_3	4.95	5.24	4.80	4.51	4.85	5.16	5.37	5.20	5.34	4.73	4.78	5.16	4.89	5.19	5.22
MnO	0.09	0.14	0.10	0.10	0.10	0.09	0.13	0.09	0.13	0.09	0.07	0.09	0.08	0.09	0.10
MgO	0.16	0.19	0.18	0.15	0.18	0.14	0.15	0.25	0.21	0.11	0.17	0.14	0.14	0.14	0.12
CaO	0.30	0.59	0.14	0.12	0.28	0.31	0.23	0.11	0.30	0.93	1.03	0.77	0.93	0.39	0.49
Na_2O	6.12	6.41	7.05	8.02	8.27	6.61	7.09	6.18	6.37	7.02	7.01	7.14	6.86	6.67	6.83
K_2O	4.76	5.10	4.11	2.85	3.16	4.92	4.63	5.19	5.00	2.87	2.93	3.76	3.47	4.00	3.78
P_2O_5	0.05	0.06	0.06	0.03	0.04	0.06	0.06	0.05	0.05	0.04	0.06	0.05	0.04	0.04	0.05
LOl	1.34	1.76	1.49	1.08	1.00	0.99	0.90	1.12	1.69	1.54	1.91	1.50	1.64	1.31	1.26
Sc	2.04	2.14	1.99	1.85	2.00	2.09	1.95	2.09	2.10	1.84	1.81	1.91	2.00	2.13	2.03
V	16.2	20.0	10.3	1.87	1.77	7.24	7.62	4.67	6.44	3.02	6.50	5.82	3.78	7.22	6.92
Cr	3.01	3.08	2.75	5.53	5.33	7.59	5.19	2.62	1.65	4.76	3.19	1.27	2.32	3.36	1.27
Co	0.15	1.15	0.12	0.11	0.13	0.13	0.15	0.17	0.11	0.28	0.35	0.19	0.20	0.37	0.38
Ni	5.96	5.51	2.46	6.05	3.01	4.80	3.36	7.19	0.43	2.54	4.18	2.83	1.96	2.35	2.93
Cu	0.49	1.46	6.30	1.28	1.02	1.28	0.74	1.08	0.83	0.58	3.80	1.48	1.65	1.56	2.13
Ga	36.3	38.9	35.8	33.2	34.9	40.2	38.1	41.7	42.2	33.7	30.4	37.8	36.4	40.6	36.5
Rb	122	136	80.8	56.8	62.9	154	138	176	169	97.2	46.4	89.6	69.7	86.8	64.3
Sr	26.3	27.5	45.2	38.6	41.9	26.2	27.6	30.3	32.9	48.3	27.7	27.7	31.3	21.3	34.4
Y	86.2	67.6	75.3	62.7	77.5	84.5	76.3	80.6	82.3	79.3	52.0	56.9	56.6	62.7	59.5
Zr	1073	1031	1077	927	1079	1122	1049	1117	1114	1047	927	1022	1008	1093	1046
Nb	209	209	182	192	206	221	213	226	225	210	172	204	209	256	201
Cs	1.43	1.79	0.84	0.86	1.24	1.82	1.77	1.99	1.99	1.52	0.79	1.25	0.99	1.06	0.94
Ba	181	178	167	147	162	193	202	195	210	135	133	124	113	153	150
La	130	131	133	141	133	139	132	138	139	131	101	103	99	106	103
Ce	251	252	248	262	258	267	255	265	265	242	185	190	181	201	191
Pr	26.8	26.3	26.4	27.8	27.2	28.3	26.7	28.2	28.0	25.9	21.4	22.2	21.4	23.2	21.9
Nd	96.5	94.1	93.2	99.1	97.3	102	95.6	101	100	92.0	69.7	73.3	70.2	76.4	70.0
Sm	18.6	17.9	17.7	17.9	18.9	19.7	18.4	19.1	19.3	17.6	12.4	13.8	13.4	14.6	12.0
Eu	2.41	2.39	2.33	2.30	2.42	2.52	2.41	2.57	2.50	2.26	1.67	1.79	1.72	1.90	1.53
Gd	17.2	16.0	16.7	15.8	17.3	18.1	16.8	17.3	17.7	16.1	11.6	12.5	12.4	13.5	11.1
Tb	2.69	2.41	2.61	2.33	2.66	2.83	2.60	2.68	2.76	2.52	1.99	2.15	2.12	2.35	1.99
Dy	16.4	14.1	15.5	13.4	15.7	16.8	15.4	16.0	16.4	15.4	11.5	12.4	12.1	13.5	11.9
Ho	3.20	2.65	2.94	2.50	2.99	3.21	2.95	3.13	3.14	3.01	2.36	2.58	2.45	2.77	2.52
Er	9.42	7.61	8.44	7.16	8.62	9.21	8.44	9.20	9.15	8.81	6.35	7.00	6.59	7.41	6.80
Tm	1.32	1.09	1.19	1.02	1.22	1.28	1.18	1.32	1.28	1.25	0.91	1.01	0.95	1.05	0.98
Yb	8.59	7.10	7.82	6.81	7.96	8.32	7.76	8.58	8.32	8.14	5.93	6.47	6.08	6.74	6.26
Lu	1.20	1.01	1.10	0.98	1.13	1.17	1.09	1.19	1.17	1.14	0.83	0.91	0.86	0.96	0.89
Hf	24.7	25.2	25.0	22.4	25.4	26.8	25.3	26.0	26.9	24.4	20.8	22.7	22.0	23.8	22.1
Ta	13.0	13.7	13.4	13.3	14.1	14.8	13.8	14.4	14.8	13.0	11.8	13.1	12.3	16.0	13.1
Pb	4.92	5.23	8.32	5.06	6.15	6.08	5.96	7.37	7.36	5.90	2.06	3.82	4.63	2.85	2.43
Th	20.0	20.4	20.0	20.3	20.7	21.3	20.1	21.0	21.5	19.3	13.6	14.0	13.5	14.8	13.7
U	1.55	1.78	2.13	1.88	2.70	1.46	1.38	1.54	1.50	1.31	0.99	1.07	0.94	1.04	0.97

Ocean; Kinman et al. 2009; Rao et al. 2014; Frey et al. 2015; Olierook et al. 2016; Watson et al. 2016), we found that the ocean islands containing phonolite are all located in mature ocean basins (i.e., the Pacific and Atlantic oceans) far from a mid-ocean ridge (Giresse and Wiewióra 1999; Marques et al. 1999; Thirlwall et al. 2000; Geldmacher et al. 2001; Rodriguez-Losada and Martinez-Frias 2004; Klügel et al. 2005; Santos and Marques 2007; Reagan et al. 2008; Chan

Table 3 Zircon LA–ICP–MS U–Pb data of the phonolite in the Nare Ocean Island

Spots	Element content (ppm)				Isotope ratio (± 1σ)						Age (Ma ± 1σ)					
	Pb	^{232}Th	238U	Th/U	^{207}Pb/^{206}Pb		^{207}Pb/^{235}U		^{206}Pb/^{238}U		^{207}Pb/^{206}Pb		^{207}Pb/^{235}U		^{206}Pb/^{238}U	
					Ratios	1σ	Ratios	1σ	Ratios	1σ	Age	Ratio	Age	1σ	Age	1σ
T1-01	12.3	267	266	1.00	0.05113	0.00105	0.26353	0.00532	0.03738	0.00044	247	26	238	4	237	3
T1-02	20.2	501	409	1.23	0.05102	0.00092	0.27052	0.00478	0.03845	0.00044	242	21	243	4	243	3
T1-03	28.3	819	539	1.52	0.05287	0.00086	0.28177	0.00449	0.03865	0.00044	323	18	252	4	244	3
T1-04	19.0	593	352	1.68	0.05118	0.00098	0.27026	0.00507	0.03829	0.00045	249	23	243	4	242	3
T1-05	10.6	237	221	1.08	0.05123	0.00118	0.27426	0.00619	0.03882	0.00046	251	31	246	5	246	3
T1-06	17.5	416	350	1.19	0.05112	0.00095	0.27487	0.00498	0.03899	0.00046	246	21	247	4	247	3
T1-07	29.5	894	556	1.61	0.05122	0.00083	0.27051	0.00427	0.0383	0.00044	251	17	243	3	242	3
T1-08	7.13	108	161	0.67	0.05108	0.00133	0.27484	0.007	0.03902	0.00048	244	36	247	6	247	3
T1-09	16.4	379	354	1.07	0.05167	0.00096	0.26224	0.00476	0.0368	0.00043	271	22	236	4	233	3
T1-10	16.1	421	324	1.30	0.05177	0.0009	0.26822	0.00455	0.03757	0.00043	275	20	241	4	238	3
T1-11	28.5	1031	505	2.04	0.05109	0.0008	0.26401	0.00403	0.03747	0.00043	245	17	238	3	237	3
T1-12	76.8	3317	1244	2.67	0.05098	0.00064	0.25806	0.00323	0.03671	0.00041	240	13	233	3	232	3
T1-13	20.3	479	425	1.13	0.05113	0.00251	0.25742	0.0122	0.03652	0.00046	247	115	233	10	231	3
T1-14	52.6	2133	890	2.40	0.05104	0.00068	0.26053	0.00345	0.03701	0.00041	243	14	235	3	234	3
T1-15	17.1	513	337	1.52	0.05106	0.00104	0.258	0.00512	0.03664	0.00043	244	25	233	4	232	3
T1-16	15.2	407	290	1.40	0.05418	0.00391	0.28271	0.01995	0.03784	0.00057	379	167	253	16	239	4
T2-01	8.28	150	182	0.82	0.05085	0.00137	0.26825	0.00702	0.03825	0.00048	234	37	241	6	242	3
T2-02	11.0	195	240	0.81	0.05098	0.00099	0.27221	0.00518	0.03872	0.00045	240	23	244	4	245	3
T2-03	17.3	443	352	1.26	0.05111	0.00095	0.26528	0.00484	0.03763	0.00044	246	22	239	4	238	3
T2-04	3.60	45.1	81.1	0.56	0.051	0.00222	0.2808	0.01196	0.03993	0.00057	241	72	251	9	252	4
T2-05	3.48	23.4	86.0	0.27	0.05118	0.00183	0.27453	0.00961	0.03889	0.00051	249	56	246	8	246	3
T2-06	12.6	358	240	1.49	0.05128	0.00117	0.27102	0.00602	0.03832	0.00046	253	30	244	5	242	3
T2-07	4.82	81.5	107	0.76	0.05111	0.00145	0.27059	0.00753	0.03839	0.00048	246	41	243	6	243	3
T2-08	13.1	281	279	1.01	0.05121	0.00094	0.26548	0.00482	0.03759	0.00043	250	22	239	4	238	3
T2-09	13.7	324	281	1.15	0.05112	0.00103	0.27406	0.00539	0.03887	0.00046	246	24	246	4	246	3
T2-10	9.54	164	209	0.79	0.05123	0.00117	0.27397	0.00612	0.03878	0.00047	251	30	246	5	245	3
T2-11	17.3	427	356	1.20	0.051	0.0009	0.2677	0.00462	0.03806	0.00044	241	20	241	4	241	3
T2-12	32.8	1411	546	2.58	0.05116	0.00076	0.2674	0.00391	0.0379	0.00043	248	16	241	3	240	3
T2-13	10.1	205	219	0.94	0.05092	0.00108	0.26513	0.00553	0.03775	0.00045	237	27	239	4	239	3
T2-14	20.9	475	417	1.14	0.05119	0.00087	0.28153	0.0047	0.03988	0.00046	249	19	252	4	252	3
T2-15	22.2	631	437	1.44	0.0509	0.0008	0.26619	0.00414	0.03792	0.00043	236	17	240	3	240	3
T2-16	9.78	199	211	0.94	0.05108	0.00123	0.27008	0.00636	0.03834	0.00046	244	32	243	5	243	3
T2-17	8.41	153	189	0.81	0.05081	0.0012	0.26215	0.00604	0.03741	0.00046	232	31	236	5	237	3
T2-18	25.2	752	478	1.57	0.05088	0.00082	0.26682	0.00423	0.03803	0.00043	235	18	240	3	241	3
T2-19	30.4	1069	552	1.93	0.0509	0.0008	0.26133	0.00404	0.03723	0.00042	236	17	236	3	236	3
T2-20	6.12	113	135	0.84	0.05103	0.00207	0.26958	0.01066	0.0383	0.00055	242	65	242	9	242	3
T2-21	16.8	394	353	1.12	0.05113	0.0012	0.2638	0.00607	0.03741	0.00045	247	31	238	5	237	3

et al. 2009; Takamasa et al. 2009; Mourão et al. 2010; Dyhr and Holm 2010; Ancochea et al. 2012; Kahn et al. 2013; Perlingeiro et al. 2013; Guillou et al. 2014; Bongiolo et al. 2015; Garcia et al. 2016; Weit et al. 2016). Moreover, all these islands formed on a thick oceanic lithosphere (Calmant and Cazenave 1986; Carracedo et al. 1998, 2002; Caplan-Auerbach et al. 2000; Burke 2001; Ingle et al. 2003; Clouard and Bonneville 2004a, b; Humphreys and Niu 2009). For example, the Canary Islands (Andújar et al. 2008; Humphreys and Niu 2009) at the eastern margin of the Atlantic Ocean, the Fernando de Noronha archipelago (Burke 2001; Perlingeiro et al. 2013) at the western margin of the Atlantic Ocean, the Trinidade Islands (Caplan-Auerbach et al. 2000; Gripp and Gordon 2002; Bongiolo et al. 2015) in the South Atlantic Ocean, and the Hawaiian archipelago in the Pacific Ocean formed on lithosphere with a thickness of 90 km,

Table 4 Trace element data of the zircon grains from phonolite samples of the Nare Ocean Island

Sample	La	Ce	Pr	Nd	Sm	Eu	Gd	Tb	Dy	Ho	Er	Tm	Yb	Lu
T2-01	0.12	23.1	0.87	17.4	29.9	4.57	114	38.2	428	129	508	98.6	1006	152
T2-02	0.06	39.2	0.29	6.58	16.5	2.68	71.9	25.1	293	91.7	373	73.6	744	115
T2-03	0.07	48.7	0.41	8.60	19.5	3.17	82.4	27.9	319	96.9	392	74.9	749	114
T2-04	0.05	10.9	0.11	2.36	4.68	0.81	21.8	8.08	100	32.8	141	28.7	301	48.5
T2-05	0.05	9.95	0.04	0.73	1.90	0.31	9.70	4.17	55.4	19.3	86.9	18.9	206	33.8
T2-06	0.04	23.6	0.24	4.83	11.7	2.66	55.0	18.2	209	65.3	261	50.7	512	82.0
T2-07	0.06	8.36	0.39	8.16	18.9	3.98	74.3	25.1	284	85.9	346	68.6	706	113
T2-08	0.08	46.5	1.81	32.0	51.8	8.12	189	61.7	684	200	802	151	1541	224
T2-09	0.63	48.0	1.40	27.7	55.4	8.23	208	67.7	749	223	890	162	1652	240
T2-10	0.03	34.7	0.32	7.38	16.1	2.71	68.6	24.1	287	89.5	366	72.2	744	116
T2-11	0.15	69.4	2.11	43.0	72.7	10.6	264	85.9	940	280	1098	201	2032	292
T2-12	0.09	94.6	0.74	18.0	40.8	7.91	158	49.6	540	155	595	109	1056	162
T2-13	0.10	33.4	1.34	24.5	39.2	6.09	145	48.3	533	159	627	120	1230	184
T2-14	0.23	101	1.62	31.4	61.5	7.59	245	84.4	969	291	1152	209	2024	286
T2-15	0.07	77.8	0.59	11.2	27.7	4.32	115	39.2	438	132	520	98.0	942	141
T2-16	0.06	34.6	0.62	12.4	25.4	4.30	99.1	33.5	382	116	468	90.0	909	142
T2-17	0.16	30.8	0.36	6.76	15.7	2.92	67.3	23.4	272	84.3	341	67.2	681	109
T2-18	0.06	70.1	0.52	11.5	26.5	4.10	106	34.8	390	114	451	85.1	842	123
T2-19	0.07	97.6	0.74	18.1	42.3	6.77	166	52.7	568	166	628	119	1153	170
T2-20	0.09	17.6	0.91	15.5	24.5	4.20	89.7	29.7	336	99.3	388	75.9	764	120
T2-21	0.15	64.1	1.76	37.5	66.4	9.78	236	78.3	859	247	950	178	1811	258
T1-01	0.11	37.0	1.09	25.1	47.4	7.15	178	57.9	634	190	742	141	1447	209
T1-02	0.06	83.9	0.58	12.9	32.7	5.17	138	46.3	515	153	606	116	1153	170
T1-03	0.44	156	4.39	77.0	121	15.1	432	138	1514	442	1659	305	2831	409
T1-04	0.09	45.2	0.44	8.93	19.7	3.94	81.2	26.6	296	90.6	358	67.6	674	105
T1-05	0.44	29.4	0.54	10.4	22.2	4.38	90.3	30.5	341	105	423	82.7	848	129
T1-06	0.13	60.8	1.34	31.0	57.4	8.92	211	68.7	761	223	890	163	1709	241
T1-07	0.06	114	0.73	19.7	43.1	6.62	172	55.2	610	180	690	128	1310	187
T1-08	0.29	23.4	0.40	6.93	14.8	2.36	61.6	22.8	280	91.4	386	78.0	798	125
T1-09	0.08	57.6	1.08	24.9	49.7	7.78	181	60.8	681	202	793	152	1575	219
T1-10	0.04	45.8	0.31	5.85	16.4	2.69	72.1	24.7	284	85.0	339	64.2	646	97.8
T1-11	0.09	81.0	0.75	16.9	35.0	6.64	133	42.2	460	134	518	95.9	964	142
T1-12	0.14	307	2.48	54.3	96.0	12.7	349	107	1144	319	1145	204	1913	245
T1-13	0.27	89.0	2.46	42.7	68.4	9.22	250	82.5	908	278	1072	195	1991	271
T1-14	0.63	206	1.64	36.4	80.7	12.3	290	88.5	922	256	975	170	1692	230
T1-15	0.10	52.0	1.26	27.2	51.0	8.47	177	56.5	626	183	706	137	1419	199
T1-16	0.08	31.5	0.35	6.03	15.2	3.51	68.5	23.0	252	75.8	311	60.1	619	96.9

and the lithosphere beneath Tristan da Cunha Island in the Atlantic Ocean is 56 km thick (Humphreys and Niu 2009; Weit et al. 2016), that under Gough Island in the Atlantic Ocean and the Society Islands in the Pacific Ocean 77 km thick (Calmant and Cazenave 1986; Caplan-Auerbach et al. 2000; Clouard and Bonneville 2004a, b; Humphreys and Niu 2009; Kahn et al. 2013), and that under the Austral–Cook archipelago in the Pacific Ocean 46–55 km thick (Clouard and Bonneville 2004b; Takamasa et al. 2009). The Middle Triassic NaOI contains significant amounts of phonolite, so the question is posed: did the NaOI form in a mature ocean on thick oceanic lithosphere?

We believe the answer to this question is yes, because the geochemistry of the NaOI phonolites is consistent with such a proposition. As stated above, the NaOI phonolites have high contents of SiO_2 (60.3–65.3 wt%), very low contents of MgO (0.11–0.25 wt%), very low $Mg^{\#}$ values (5–10), and near-zero contents of Cr (1.27–7.59 ppm), Ni (0.43–7.19 ppm), and Co (0.11–0.38 ppm), and in the chondrite-normalized REE variation diagram and the primitive

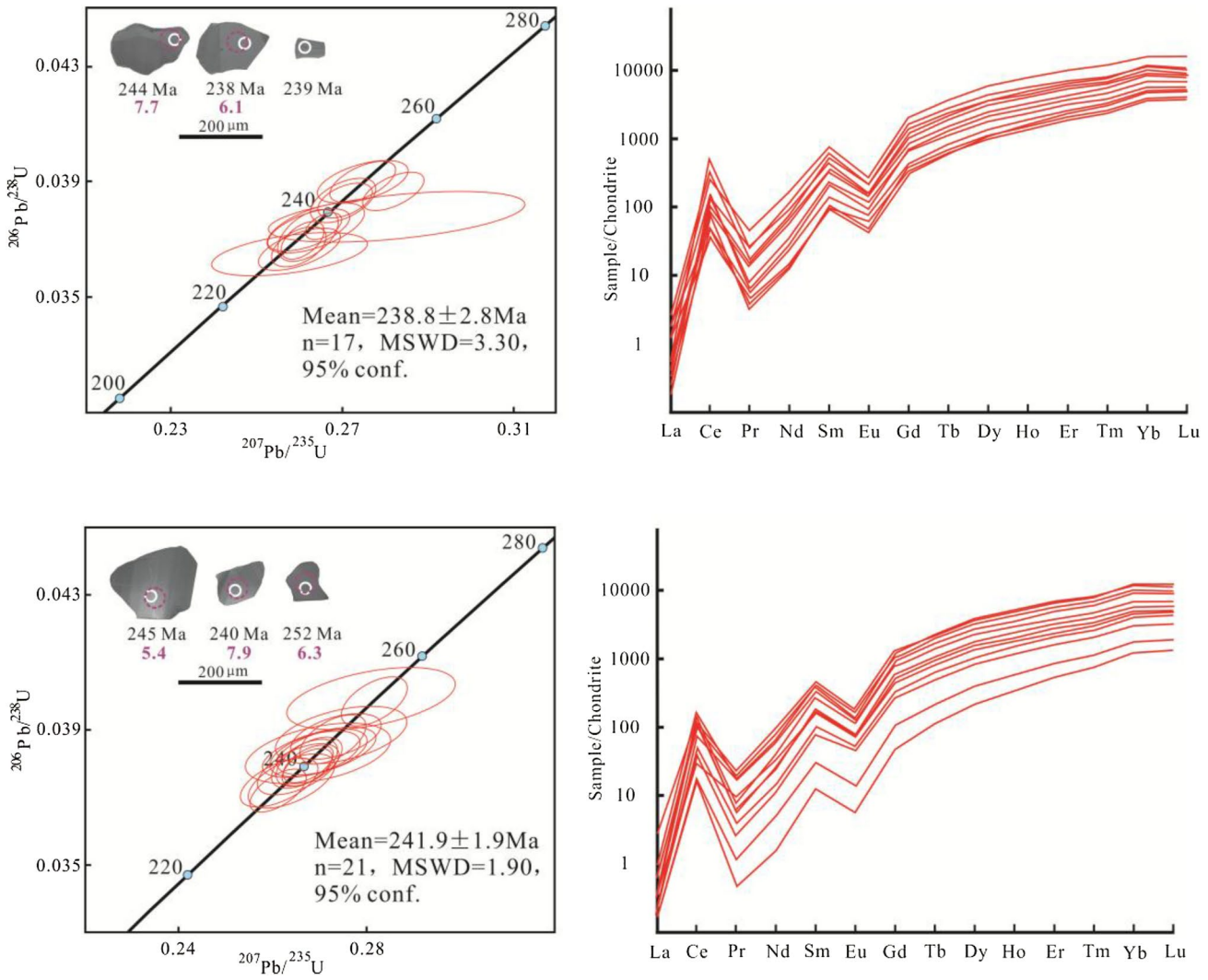

Fig. 6 CL images of zircons and concordia diagrams showing the results of LA–ICP–MS analyses of zircons from the NaOI phonolites

mantle-normalized trace element variation diagram (Fig. 4a, b) they exhibit a series of very low negative anomalies (e.g., Eu, Ba, U, K, Sr, P, and Ti), indicating that their parental magma underwent substantial fractional crystallization of plagioclase, apatite, Fe–Ti oxides, and feldspar during ascent. Such a substantial fractional crystallization of the parental NaOI phonolite magma would have been facilitated by a lengthy ascent of the magma together with a long cooling process. In other words, fractional crystallization would have been greatly enhanced if the magma was emplaced into thick oceanic lithosphere.

Based on our survey of modern ocean islands and our geochemical data for the NaOI phonolites, we conclude, therefore, that the Middle Triassic NaOI was formed in a mature ocean basin with a thick underlying oceanic lithosphere.

According to the theory of plate tectonics, oceanic lithosphere initially forms at a mid-ocean ridge and becomes gradually cooler and thicker as it moves away from the ridge (Oxburgh and Parmentier 1977). The thickness of the oceanic lithosphere can be determined from the age of the lithosphere using the half-space lithosphere cooling model ($T = 11 \times t^{1/2}$ where T is lithosphere thickness in km, and t is the age in Ma). The model is reliable for lithosphere younger than ~ 70 Ma (Parsons and Sclater 1977; Phipps Morgan and Smith 1992; Stein and Stein 1992). Because oceanic lithosphere reaches its full thickness at an age of ~ 70 Myr, we assume a constant thickness of ~ 90 km (i.e., $11 \times 70^{1/2}$ = 92 km) for older lithosphere (Humphreys and Niu 2009).

Table 5 Zircon Hf isotopic composition of the rhyolite samples of the Zhaga Formation

No.	Age (Ma)	$^{176}Yb/^{177}Hf$	2δ	$^{176}Lu/^{177}Hf$	2δ	$^{176}Hf/^{177}Hf$	2δ	$\varepsilon_{Hf}(0)$	$\varepsilon_{Hf}(t)$	2δ	T_{DM} (Ma)	T^{C}_{DM} (Ma)	$f_{Lu/Hf}$
T1-01	239	0.167070	0.000889	0.004254	0.000019	0.282847	0.000026	2.7	7.2	0.9	629	806	−0.87
T1-02	239	0.130928	0.000204	0.003295	0.000012	0.282857	0.000021	3.0	7.7	0.8	597	775	−0.90
T1-03	239	0.135055	0.000391	0.003410	0.000010	0.282829	0.000021	2.0	6.7	0.7	642	840	−0.90
T1-04	239	0.096452	0.002384	0.002580	0.000080	0.282859	0.000021	3.1	7.9	0.7	582	763	−0.92
T1-05	239	0.140500	0.003237	0.003575	0.000079	0.282909	0.000021	4.8	9.5	0.7	522	660	−0.89
T1-06	239	0.092887	0.001788	0.002428	0.000035	0.282808	0.000022	1.3	6.1	0.8	654	876	−0.93
T1-07	239	0.128666	0.001225	0.003233	0.000036	0.282778	0.000021	0.2	4.9	0.7	716	953	−0.90
T2-01	242	0.105046	0.000246	0.002675	0.000005	0.282785	0.000020	0.5	5.4	0.7	693	928	−0.92
T2-02	242	0.080808	0.000164	0.002114	0.000008	0.282784	0.000021	0.4	5.4	0.7	685	926	−0.94
T2-03	242	0.056723	0.000225	0.001494	0.000005	0.282825	0.000020	1.9	6.9	0.7	615	828	−0.96
T2-04	242	0.023533	0.001835	0.000571	0.000043	0.282789	0.000017	0.6	5.8	0.6	649	899	−0.98
T2-05	242	0.073521	0.000666	0.001954	0.000021	0.282825	0.000021	1.9	6.9	0.7	622	832	−0.94
T2-06	242	0.127001	0.000274	0.003271	0.000002	0.282860	0.000022	3.1	7.9	0.8	592	766	−0.90
T2-07	242	0.281883	0.004295	0.007279	0.000163	0.282919	0.000031	5.2	9.4	1.1	567	673	−0.78
T2-08	242	0.200189	0.002156	0.005346	0.000082	0.282878	0.000025	3.8	8.2	0.9	600	746	−0.84
T2-09	242	0.209858	0.001107	0.005218	0.000008	0.282881	0.000024	3.9	8.3	0.8	592	737	−0.84
T2-10	242	0.064912	0.000209	0.001648	0.000003	0.282809	0.000018	1.3	6.3	0.6	640	866	−0.95

Corrected formula as follows (Chu et al. 2006)

$\varepsilon_{Hf}(t) = [(^{176}Hf/^{177}Hf)_{Sample}(T)/(^{176}Hf/^{177}Hf)_{CHUR}(T) - 1] \times 10^4$

$T_{DM} = 1/\lambda * \ln\{1 + [((^{176}Hf/^{177}Hf)_{sample} - (^{176}Hf/^{177}Hf)_{DM})/((^{176}Lu/^{177}Hf)_{sample} - (^{176}Lu/^{177}Hf)_{DM})]\}$

$T^{C}_{DM}\,(Hf) = T_{DM} - (T_{DM} - T) \times [(f_{CC} - f_S)/(f_{CC} - f_{DM})]$

$f_{Lu/Hf} = [(^{176}Lu/^{177}Hf)_{sample}/(^{176}Lu/^{177}Hf)_{CHUR}] - 1$

The Middle Triassic NaOI formed on a thick oceanic lithosphere, indicating that at least during the Middle Triassic the BNTO has had a thick oceanic lithosphere. According to the half-space model of lithosphere cooling, the thick oceanic lithosphere of the BNTO during the Middle Triassic indicates that the BNTO had already been open, for a long time before the Middle Triassic. This inference is further supported by the following lines of evidence. (1) Early to Middle Triassic radiolarian cherts and Late Permian–Early Triassic eclogites have been documented in the BNSZ (Pan et al. 2006; Zhang et al. 2016); (2) Detailed geochemical studies for the basalts of the Late Triassic Gufeng ocean island fragment in the western segment of the BNSZ has showed that the BNTO has opened at least during the late Permian (Fan et al. 2017).

In summary, we conclude that the BNTO opened long before the Middle Triassic and that this ocean had developed into a mature ocean with a thick oceanic lithosphere by at least the Middle Triassic.

Fig. 7 **a** Sm/Yb vs. La/Sm diagram for the NaOI basalts (modified after Zhao and Zhou 2007). The mantle array (heavy line) is defined by depleted MORB mantle (DM; McKenzie and O'Nions 1991) and primitive mantle (PM; Sun and McDonough 1989). Melting curves for spinel lherzolite and garnet peridotite with both DM and PM compositions are after Aldanmaz et al. (2000). Numbers along lines represent the degrees of partial melting. **b–f** Variation diagrams for the NaOI basalt samples

Conclusions

1. The NaOI basalts were derived from the partial melting of garnet peridotite in the mantle, and the ascending magmas underwent varying degrees of fractional crystallization but were not contaminated by the crust.
2. The NaOI phonolites were formed by fractional crystallization of OIB-type parental magma. In common with the NaOI basalts, the ascending NaOI phonolite magmas were not contaminated by the crust.

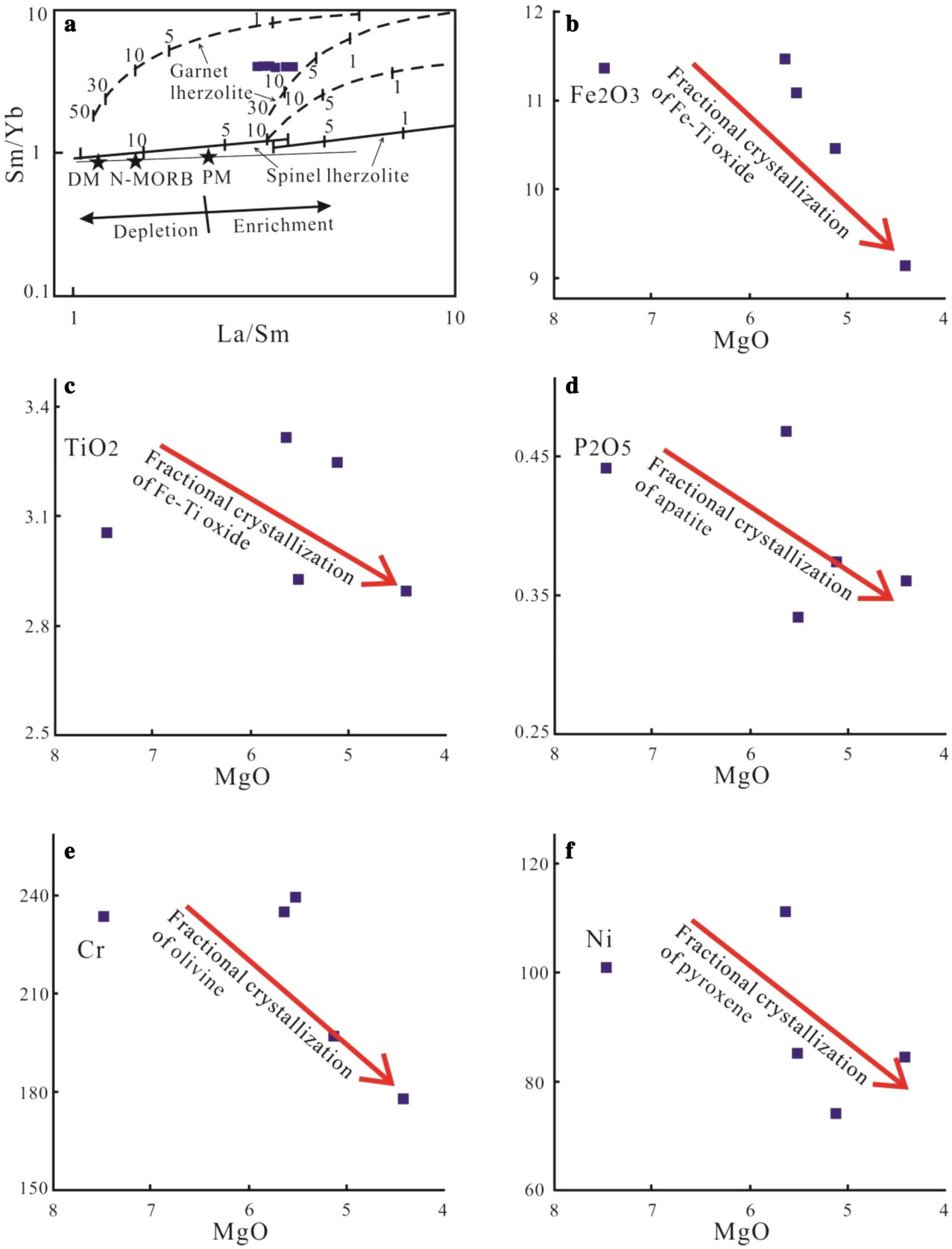
a
Sm/Yb
La/Sm
Garnet lherzolite
Spinel lherzolite
DM N-MORB PM
Depletion
Enrichment
b
Fe2O3
Fractional crystallization of Fe-Ti oxide
MgO
c
TiO2
Fractional crystallization of Fe-Ti oxide
MgO
d
P2O5
Fractional crystallization of apatite
MgO
e
Cr
Fractional crystallization of olivine
MgO
f
Ni
Fractional crystallization of pyroxene
MgO

3. The Middle Triassic NaOI is a typical ocean island that formed within a mature ocean basin with a thick oceanic lithosphere.
4. The Bangong–Nujiang Tethyan Ocean opened long before the Middle Triassic, and the ocean had developed into a mature ocean by at least the Middle Triassic.

Acknowledgements We thank Mr. Hao Wu, Mr. Tianyu Zhang, Mr Qiangyuan Jiang, and Mr. Jianxin Xu for their help in the field. This research was supported by the National Science Foundation of China (Grant no. 41702227), the National Postdoctoral Program for Innovative Talents (Grant no. BX201600061), China Postdoctoral Science Foundation (Grant no. 2017M610192), and the China Geological Survey project (Grant nos. DD20160026 and 1212010100001500l4).

References

Ackerman L, Ulrych J, Řanda Z, Erban V, Hegner E, Magna T, Balogh K, Frána J, Lang M, Novák J (2015) Geochemical characteristics and petrogenesis of phonolites and trachytic rocks from the České Středohoří Volcanic Complex, the Ohře Rift, Bohemian Massif. Lithos 224–225:256–271

Aldanmaz E, Pearce JA, Thirlwall MF, Mitchell JG (2000) Petrogenetic evolution of late Cenozoic, post-collision volcanism in western Anatolia, Turkey. J Volcanol Geoth Res 102:67–95

Allègre CJ, Courtillot V, Tapponnie P et al (1984) Structure and evolution of the Himalaya–Tibet orogenic belt. Nature 307:17–22

Ancochea E, Hernán F, Huertas MJ, Brändle JL (2012) A basic radial dike swarm of Boa Vista (Cape Verde Archipelago); its significance in the evolution of the island. J Volcanol Geoth Res 243–244:24–37

Anderson T (2002) Correction of common lead in U–Pb analyses that do not report ^{204}Pb. Chem Geol 192:59–79

Andújar J, Costa F, Martí J, Wolff JA, Carroll MR (2008) Experimental constraints on pre-eruptive conditions of phonolitic magma from the caldera-forming El Abrigo eruption, Tenerife (Canary Islands). Chem Geol 257:173–190

Baker BH, McBirney AR (1985) Liquid fractionation. Part III: Geochemistry of zoned magmas and the compositional effects of liquid fractionation. J Volcanol Geoth Res 24:55–81

Bao PS, Xiao XC, Su L, Wang J (2007) Geochemical characteristics and isotopic dating for the Dongcuo ophiolite, Tibet Plateau. China Sci (D) 50:660–671 **(Chinese with English abstract)**

Barberi F, Ferrara G, Santacroce R, Treuil M, Varet J (1975) Transitional basalt-pantellerite sequence of fractional crystallization, Boina crater (Afar rift, Ethiopia). J Petrol 16:22–56

Beattie P (1994) Systematics and energetics of trace–element partitioning between olivine and silicate melts: implications for the nature of mineral/melt partitioning. Chem Geol 117:57–71

Bongiolo EM, Pires GLC, Geraldes MC, Santos AC, Neumann R (2015) Geochemical modeling and Nd–Sr data links nephelinite–phonolite successions and xenoliths of Trindade Island (South Atlantic Ocean, Brazil). J Volcanol Geoth Res 306:58–73

Bureau of Geology and Mineral Exploration of Tibet Province (1993) Regional geology of Tibet Province. Geological Publishing House, Beijing, pp 1–707 **(in Chinese with English abstract)**

Burke K (2001) Origin of the Cameroon line of volcano-capped swells. J Geol 109:349–362

Calmant S, Cazenave A (1986) The effective elastic lithosphere under the Cook-Austral and Society islands. Earth Planet Sc Lett 77:187–202

Caplan-Auerbach J, Dunnebier F, Ito G (2000) Origin of intraplate volcanoes from guyot heights and oceanic paleodepth. J Geophys Res 105:2679–2697

Carracedo JC, Day S, Guillou H, Rodriguez Badiolas ER, Canas JA, Perez Torrado FJ (1998) Hotspot volcanism close to a passive continental margin: the Canary Islands. Geol Mag 135:591–604

Carracedo JC, Pérez FJ, Ancochea E, Meco J, Hernán F, Cubas CR, Casillas R, Rodriguez E, Ahijado A (2002) Cenozoic volcanism II: the Canary Islands. In: Gibbons W, Moreno T (eds), The geology of Spain. Geological Society of London, London, pp 439–472

Chan LH, Lassiter JC, Hauri EH, Hart SR, Blusztajn J (2009) Lithium isotope systematics of lavas from the Cook–Austral Islands: constraints on the origin of HIMU mantle. Earth Planet Sci Lett 277:433–442

Chang CF (1978) Geological evolution history of the Himalayas; outline of the tectonic belt and discussion of the cause of uplift. International Geological Symposium (1): Tectonics and Geomechanics. Geological Publishing House, Beijing, pp 198–211 **(in Chinese)**

Chang CF, Zhen XK (1973) Tectonic characteristics of Qomolangma area in southern Tibet, China and discussion of the formation of E–W extending mountains in Tibet Plateau. Geosciences 2:1–12 **(Chinese)**.

Chu MF, Chung SL, Song B, Liu DY, O'Reilly SY, Pearson NJ, Ji JQ, Wen DJ (2006) Zircon U-Pb and Hf isotope constraints on the Mesozoic tectonics and crustal evolution of southern Tibet. Geology 34:745–748

Clouard V, Bonneville A (2004a) Ages of Seamounts, Islands and Plateaus on the Pacific Plate. Version 2.1. http://www.mantleplumes.org

Clouard V, Bonneville A (2004b) In: Hekinian R (ed), Importance of submarine landslides in French Polynesia. Springer, Oceanic Hotspots, pp 209–238

Condie KC (1993) Chemical composition and evolution of the upper continental crust: contrasting results from surface samples and shales. Chem Geol 104:1–37

Dewey JF, Shackelton RM, Chang C, Sun Y (1988) The tectonic evolution of the Tibetan plateau. Philos Trans R Soc Lond A327:379–413

Dyhr CT, Holm PM (2010) A volcanological and geochemical investigation of Boa Vista, Cape Verde Islands; ^{40}Ar/^{39}Ar geochronology and field constraints. J Volcanol Geoth Res 189:19–32

Enders M, Laemmlen M, Förster H (1992) Polybaric differentiation of alkaline volcanic rocks in the Rhön Mountains, Hessia, Germany: evidence from trace-element distribution. Chemie der Erde Geochemistry 52:189–203

Fan JJ, Li C, Xu JX, Wang M (2014a) Petrology, geochemistry and geological significance of the Nadong ocean island, Banggong–Nujiang suture, Tibetan Plateau. Int Geol Rev 56:915–928

Fan JJ, Li C, Xie CM, Wang M (2014b) Petrology, geochemistry, and geochronology of the Zhonggang ocean island, northern Tiber: implications for the evolution of the Bangongco–Nujiang oceanic arm of Neo-Tethys. Int Geol Rev 56:1504–1520

Fan JJ, Li C, Liu YM, Xu JX (2015a) Age and nature of the late Early Cretaceous Zhaga Formation, northern Tibet: constraints on when the Bangong–Nujiang Neo-Tethys Ocean closed. Int Geol Rev 57:342–353

Fan JJ, Li C, Xie CM, Wang M, Chen JW (2015b) The evolution of the Bangong–Nujiang Neo-Tethys ocean: evidence from zircon U–Pb and Lu–Hf isotopic analyses of Early Cretaceous oceanic islands and ophiolites. Tectonophysics 655:27–41

Fan JJ, Li C, Wang M, Liu YM, Xie CM (2017) Remnants of a Late Triassic ocean island in the Gufeng area, northern Tibet: implications for the opening and early evolution of the Bangong–Nujiang Tethyan Ocean. J Asian Earth Sci 135:35–50

Frey FA, Green DH, Roy SD (1978) Integrated models of basalt petrogenesis: a study of quartz tholeiites to olivine melilitites from South Eastern Australia utilizing geochemical and experimental petrological data. J Petrol 19:463–513

Frey FA, Silva IGN, Huang S, Pringle MS, Meleney PR, Weis D (2015) Depleted components in the source of hotspot magmas: evidence from the Ninetyeast Ridge (Kerguelen). Earth Planet Sci Lett 426:293–304

Garcia MO, Weis D, Jicha BR, Ito G, Hanano D (2016) Petrology and geochronology of lavas from Ka'ula Volcano: implications for rejuvenated volcanism of the Hawaiian mantle plume. Geochim Cosmochim Acta 185:278–301

Geldmacher J, Hoernle K, Bogaard P, Zankl G, Garbe-Schönberg D (2001) Earlier history of the ≥ 70-Ma-old Canary hotspot based on the temporal and geochemical evolution of the Selvagen Archipelago and neighboring seamounts in the eastern North Atlantic. J Volcanol Geoth Res 111:55–87

Girardeau J, Marcoux J, Allegre CJ, Bassoullet JP, Tang YK, Xiao XC, Zao YG, Wang XB (1984) Tectonic environment and geodynamic significance of the Neo-Cimmenian Dongqiao ophiolite, Bangong–Nujiang suture zone, Tibet. Nature 307:27–31

Giresse P, Wiewióra A (1999) Origin and diagenesis of blue-green clays and volcanic glass in the Pleistocene of the Côte d'Ivoire–Ghana Marginal Ridge (ODP Leg 159, Site 959). Sediment Geol 127:247–269

Goolaerts A, Mattielli N, de Jong J, Weis D, Scoates JS (2004) Hf and Lu isotopic reference values for the zircon standard 91500 by MC–ICP–MS. Chem Geol 206:1–9

Govindaraju K (1994) Compilation of working values and sample description for 383 geostandards. Geostand Newsl 18:1–158

Gripp AE, Gordon RG (2002) Young tracks of hotspots and current plate velocities. Geophys J Int 150:321–361

Guillou H, Maury RC, Guile G, Chauvel C, Rossi P, Pallares C, Legendre C, Blais S, Liorzou C, Deroussi S (2014) Volcanic successions in Marquesas eruptive centers: a departure from the Hawaiian model. J Volcanol Geoth Res 276:173–178

Hart SR, Dunn T (1993) Experimental cpx/melt partitioning of 24 trace elements. Contrib Miner Pet 113:1–8

Hauri EH, Wagner TP, Grove TL (1994) Experimental and natural partitioning of Th, U, Pb and other trace elements between garnet. Clinopyroxene and basaltic melts. Chem Geol 117:149–166

Hess PC (1992) Phase equilibria constraints on the origin of ocean floor basalts. Geophys Monogr 71:67–102

Hishashi K (1954) Geology and petrology of O-Shima Volcano. Int Geol Rev 1:48–59

Horn I, Foley SF, Jackson SE, Jenner GA (1994) Experimentally determined partitioning of high field strength and selected transition elements between spinel and basaltic melt. Chem Geol 117:193–218

Hoskin PWO, Black LP (2000) Metamorphosed zircon group by solid-state recrystallization of protolith igneous zircon. J Metamorph Geol 18:423–439

Hu ZC, Liu YS, Gao S, Liu WG, Zhang W, Tong XR, Lin L, Zong KQ, Li M, Chen HH, Zhou L, Yang L (2012) Improved in situ Hf isotope ratio analysis of zircon using newly designed X skimmer cone and Jet sample cone in combination with the addition of nitrogen by laser ablation multiple collector ICP–MS. J Anal Atom Spectrom 27:1391–1399

Huang QS, Shi RD, Ding BH, Liu DL, Zhang XR, Fan SQ, Zhi XC (2012) Re-Os isotopic evidence of MOR-type ophiolite from the Bangong Co for the opening of Bangong-Nujiang Tethys Ocean. Acta Petrologica et Mineralogica 21:465–478 **(Chinese with English abstract)**

Humphreys ER, Niu YL (2009) On the composition of ocean island basalts (OIB): the effects of lithospheric thickness variation and mantle metasomatism. Lithos 112:118–136

Ingle S, Weis D, Doucet S, Mattielli N (2003) Hf isotope constraints on mantle sources and shallow-level contaminants during Kerguelen hot spot activity since ~ 120 Ma. Geochem Geophys Geosyst. https://doi.org/10.1029/2002GC000482

Irvine TN, Baragar WAR (1971) A guide to the chemical classification of the common volcanic rocks. Can J Earth Sci 8:523–548

Johnson KTM (1994) Experimental cpx/ and garnet/melt partitioning of REE and other trace elements at high pressures; petrogenetic implications. Miner Mag 58:454–455

Jung S, Mezger K, Hauff F, Pack A, Hoernes S (2013) Petrogenesis of rift-related tephrites, phonolites and trachytes (Central European Volcanic Province, Rhön, FRG): constraints from Sr, Nd, Pb and O isotopes. Chem Geol 354:203–215

Kahn JG, Sinton J, Mills PR, Lundblad SP (2013) X-ray fluorescence analysis and intra-island exchange in the Society Island archipelago (Central Eastern Polynesia). J Archaeol Sci 40:1194–1202

Kapp P, Murphy MA, Yin A, Harrison TM, Ding L, Guo JH (2003) Mesozoic and Cenozoic tectonic evolution of the Shiquanhe area of western Tibet. Tectonics 22:3–23

Kapp P, DeCelles PG, Gehrels GE, Heizler M, Ding L (2007) Geological records of the Lhasa–Qiangtang and Indo–Asian collisions in the Nima area of central Tibet. Geol Soc Am Bull 119:917–932

Kinman WS, Neal CR, Davidson JP, Font L (2009) The dynamics of Kerguelen Plateau magma evolution: new insights from major element, trace element and Sr isotope microanalysis of plagioclase hosted in Elan Bank basalts. Chem Geol 264:247–265

Klügel A, Hansteen TH, Galipp K (2005) Magma storage and underplating beneath Cumbre Vieja volcano, La Palma (Canary Islands). Earth Planet Sci Lett 236:211–226

Li C, Huang XP, Zhai QG, Zhu TX, Yu YS, Wang GH, Zeng QG (2006) The Longmu Co–Shuanghu–Jitang plate suture and the northern boundary of Gondwanaland in the Qinghai–Tibet plateau. Earth Sci Front 13:136–147 **(Chinese with English Abstract)**

Li JF, Xia B, Wang R, Liu WL (2013) Mineralogical Characteristics of the Dong Tso Ophiolite and its Tectonic Implications. Geotectonica et Metallogenia 37:308–319 **(Chinese with English abstract)**

Liu YS, Gao S, Hu ZC, Gao CG, Zong KQ, Wang DB (2010) Continental and oceanic crust recycling-induced melt–peridotite interactions in the Trans-North China Orogen: U–Pb dating, Hf isotopes and trace elements in zircons from mantle xenoliths. J Petrol 51:537–571

Liu DL, Huang QS, Fan SQ, Zhang LY, Shi RD, Ding L (2014) Subduction of the Bangong–Nujiang Ocean: constraints from granites in the Bangong Co area, Tibet. Geol J 49:188–206

Lu SW, Ren JD, Du FG, Liu PD (2003) Tectonic evolution of the Meso–Tethyan Ocean: an example from the Nyima region in Xizang. Sedim Geol Tethyan Geol 23:35–39 **(Chinese with English abstract)**

Ludwig KJ (2003) ISOPLOT 3.0. Berkeley Geochronol Center Spec Publ 4:70

Macciotta G, Almeida A, Barbieri MA, Beccaluva L, Brotzu P, Coltorti M, Conte A, Garbarino C, Gomes CB, Morbidelli L, Ruberti E, Siena F, Traversa G (1990) Petrology of the tephrite-phonolite suite and cognate xenoliths from Fortaleza district (Ceara, Brazil). Eur J Miner 2:687–709

Marques LS, Ulbrich MNC, Ruberti E, Tassinari CG (1999) Petrology, geochemistry and Sr–Nd isotopes of the Trindade and Martin Vaz volcanic rocks (Southern Atlantic Ocean). J Vol Geoth Res 93:191–216

McKenzie D, O'Nions RK (1991) Partial melt distributions from inversion of rare Earth element concentrations. J Petrol 32:1021–1091

Meschede M (1986) A method of discriminating between different types of mid-ocean ridge basalts and continental tholeiites with the Nb–Zr–Y diagram. Chem Geol 56:207–218

Mourão C, Mata J, Doucelance R, Madeira J, Brum da Silveira A, Silve LC, Moreira M (2010) Quaternary extrusive calciocarbonatite volcanism on Brava Island (Cape Verde): a nephelinite–carbonatite immiscibility product. J Afr Earth Sci 56:59–74

Niu YL (2009) Some basic concepts and problems on the petrogenesis of intra-plate ocean island basalts. Chin Sci Bull 54:418–4160

Olierook HKH, Jourdan F, Merle RE, Timms NE, Kusznir N, Muhling JR (2016) Bunbury Basalt: Gondwana breakup products or earliest vestiges of the Kerguelen mantle plume? Earth Planet Sci Lett 440:20–32

Oxburgh ER, Parmentier EM (1977) Compositional and density stratification in oceanic lithosphere-causes and consequences. J Geol Soc Lond 133:343–355

Pan GT, Chen ZL, Li XZ, Yang YJ, Xu XS, Xu Q, Jiang XS, Wu YL, Luo JN, Zhu TX, Peng YM (1997) Geological–tectonic evolution in the eastern Tethys. Geological Publishing House, Beijing, pp 1–218 **(Chinese with English abstract)**

Pan GT, Mo XX, Hou ZQ, Zhu DC, Wang LQ, Li GM, Zhao ZD, Geng QR, Liao ZL (2006) Spatial–temporal framework of the Lhasa Orogenic Belt and its evolution. Acta Petrologica Sinica 22:521–533 (**Chinese with English abstract)**

Pan GT, Wang LQ, Li RS, Yuan SH, Ji WH, Yin FG, Zhang WP, Wang BD (2012) Tectonic evolution of the Qinghai–Tibet Plateau. J Asian Earth Sci 53:3–14

Parsons B, Sclater JG (1977) An analysis of the variation of ocean floor bathymetry and heat flow with age. J Geophys Res 82:803–827

Pearce JA, Cann JR (1973) Tectonic setting of basic volcanic rocks determined using trace element analyses. Earth Planet Sci Lett 19:290–300

Pearce JA (1983) The role of sub-continental lithosphere in magmagenesis at destructive plate margins. In: Hawkesworth CJ et al (eds), Continental basalts and mantle xenoliths. Nantwich Shiva, Cheshire, pp 230–249

Perlingeiro G, Vasconcelos PM, Knesel KM, Thiede DS, Cordani UG (2013) $^{40}Ar/^{39}Ar$ geochronology of the Fernando de Noronha Archipelago and implications for the origin of alkaline volcanism in the NE Brazil. J Volcanol Geoth Res 249:140–154

Phipps Morgan J, Smith WFS (1992) Flattening of the sea-floor depth-age curve as a response to asthenospheric flow. Nature 359:524–527

Qiu RZ, Zhou S, Deng JF, Li JF, Xiao QH, Cai ZY (2004) Dating of gabbro in the Shemalagou ophiolite in the western segment of the Bangong Co–Nujiang ophiolite belt, Tibet—with a discussion of the age of the Bangong Co–Nujiang ophiolite belt. Geological China 31:262–268 **(Chinese with English abstract)**

Qu XM, Xin HB, Zhao YY, Wang RJ, Fan HT (2010) Opening time of Bangong Lake Middle Tethys oceanic basin of the Tibet Plateau: constraints from petro-geochemistry and zircon U–Pb LAICPMS dating of mafic ophiolites. Earth Sci Front 17:53–63 **(Chinese with English abstract)**

Rao NVC, Srivastave RK, Sinha AK, Ravikant V (2014) Petrogenesis of Kerguelen mantle plume-linked Early Cretaceous ultrapotassic intrusive rocks from the Gondwana sedimentary basins, Damodar Valley, Eastern India. Earth Sci Rev 136:96–120

Reagan MK, Turner S, Legg M, Sims KWW, Hards VL (2008) ^{238}U- and ^{232}Th-decay series constraints on the timescales of crystal fractionation to produce the phonolite erupted in 2004 near Tristan da Cunha, South Atlantic Ocean. Geochim Cosmochim Acta 72:4367–4378

Ren JS, Xiao LW (2004) Lifting the mysterious veil of the tectonics of the Qinghai-Tiber Plateau by 1:250000 geological mapping. Geol Bull China 23:1–11 **(Chinese with English abstract)**

Rodriguez-Losada JA, Martinez-Frias J (2004) The felsic complex of the Vallehermoso Caldera: interior of an ancient volcanic system (La Gomera, Canary Islands). J Volcanol Geoth Res 137:261–284

Rudnick RL, Gao S (2003) Composition of the continental crust. Treatise Geochem 3:1–64

Santos RN, Marques LS (2007) Investigation of ^{238}U–^{230}Th–^{226}Ra and ^{232}Th–^{228}Ra–^{228}Th radioactive disequilibria in volcanic rocks from Trindade and Martin Vaz Islands (Brazil; Southern Atlantic Ocean). J Volcanol Geoth Res 161:215–233

Schwandt CS, McKay GA (1998) Rare earth element partition coefficients from enstatite/melt synthesis experiments. Geochim Cosmochim Acta 62:2845–2848

Shi RD, Yang JS, Xu ZQ, Qi XX (2008) The Bangong Lake ophiolite (NW Tibet) and its bearing on the tectonic evolution of the Bangong–Nujiang suture zone. J Asian Earth Sci 32:438–457

Smith AB, Xu JT (1988) Paleontology of the 1985 Tibet geotraverse, Lhasa to Golmud. The Geological Evolution of Tibet, A327. Philosophical Transactions of the Royal Society, London, pp 53–106

Stein CA, Stein S (1992) A model for the global variation in oceanic depth and heat flow with lithospheric age. Nature 359:123–129

Sun SS, McDough WF (1989) Chemical and isotope systematics of oceanic basalts: implications for mantle composition and processes. In: Saunders AD (ed) Magmatism in ocean Basins, vol 42. Geological Society Publication, London, pp 313–345

Takamasa A, Nakai S, Sahoo Y, Hanyu T, Tatsumi Y (2009) W isotope compositions of oceanic islands basalts from French Polynesia and their meaning for core–mantle interaction. Chem Geol 260:37–46

Thirlwall MF, Singer BS, Marriner GF (2000) ^{39}Ar–^{40}Ar ages and geochemistry of the basaltic shield stage of Tenerife, Canary Islands, Spain. J Volcanol Geoth Res 103:247–297

Vieten K, Hamm HM, Grimmeisen W (1988) Tertiärer Vulkanismus des Siebengebirges. Fortschr Mineral 66:1–42

Wang J (2000) Geological feature of the eastern sector of the Bangong Co-Nujiang River suture zone: Tethyan evolution. Acta Geol Sin 74:229–235

Wang GM, Zhong JH (2002) Tectonic sedimentary evolution of the west segment of the Bangong Co-Nujiang structural belt in the Triassic and Jurassic. Geol Rev 48:297–303 **(Chinese with English abstract)**

Wang XB, Bao PS, Deng WM (1987) Tibetan ophiolite. Geological Publishing House, Beijing, pp 1–124 **(Chinese with English abstract)**

Wang YJ, Wang JP, Liu YM, Li QS, Pei F (2002) Characteristics and age of the Dingqing ophiolite in Xizang (Tibet) and their geological significance. Acta Micropalaeontol Sin 19:417–420 **(in Chinese with English abstract)**

Wang WL, Aitchison JC, Lo CH (2008) Geochemistry and geochronology of the amphibolite blocks in ophiolitic mélange along Bangong–Nujing Suture, Central Tibet. J Asian Earth Sci 33:122–138

Wang LQ, Pan GT, Ding J, Yao DS, Luo JN (2013) The geological map and instruction of the Tibetan Plateau and its adjacent areas. Geological Publishing House, London, pp 1–288

Wang BD, Wang LQ, Chung SL, Chen JL, Yin FG, Liu H, Li XB, Chen LK (2016) Evolution of the Bangong–Nujiang Tethyan ocean: insights from the geochronology and geochemistry of mafic rocks within ophiolites. Lithos 245:18–33

Watson SJ, Whittaker JM, Halpin JA, Williams SE, Milan LA, Daczko NR, Wyman DA (2016) Tectonic drivers and the influence

of the Kerguelen plume on seafloor spreading during formation of the early Indian Ocean. Gondwana Res 35:97–114

Weit A, Trumbull RB, Keiding JK, Geissler WH, Gibson SA, Veksler IV (2016) The magmatic system beneath the Tristan da Cunha Island: insights from thermobarometry, melting models and geophysics. Tectonophysics. https://doi.org/10.1016/j.tecto.2016.08.010

Wiedenbeck M, Allé P, Corfu F, Griffin WL, Meier M, Oberli F, Quadt AV, Roddick JC, Spiegel W (1995) Three natural zircon standards for U–Th–Pb, Lu–Hf, trace element and REE analyses. Geostand Geoanal Res 19:1–23

Winchester JA, Flody PA (1977) Geochemical magma type discrimination: application to altered and metamorphosed basic igneous rocks. Earth Planet Sci Lett 28:459–469

Woodhead J, Hergt J, Shelley M, Eggins S, Kemp R (2004) Zircon Hf-isotope analysis with an excimer laser, depth profiling, ablation of complex geometries, and concomitant age estimation. Chem Geol 209:121–135

Xia B, Xu LF, Wei ZQ, Zhang YQ, Wang R, Li JF, Wang YB (2008) SHRIMP zircon dating of gabbro from the Donqiao Ophiolite in Tibet and its geological implications. Acta Geological Sinica 82:528–531 **(Chinese with English abstract)**

Xu W, Xu MJ, Wu YW, Fan JJ, Wu H (2015) Petrology geochemistry and geochronology of boninitic dykes from the Kangqiong ophiolite: implications for the Early Cretaceous evolution of Bangong–Nujiang Neo-Tethys Ocean in Tibet. Int Geol Rev 57:2028–2043

Yin JX (1997) Stratigraphy and Geology of Gondwana Facies in Qinghai–Xizang Plateau and Its Adjacent Areas. Science, Beijing, p 201 **(Chinese)**

Yin A, Harrison TM (2000) Geologic evolution of the Himalayan–Tibetan orogen. Annu Rev Earth Pl Sc 28:211–280

Yong YY, Jia BJ (2000) Shear convergence of plates and suturing of terrenes: a new model for the comsumption of the Meso-Tethys. Sedim Geol Tethyan Geol 20:85–89 **(Chinese with English abstract)**

Yuan HL, Gao S, Liu XM, Li HM, Günther D, Wu FY (2004) Accurate U–Pb age and trace element determinations of zircon by laser ablation-inductively coupled plasma mass spectrometry. Geostand Geoanal Res 28:353–370

Zeng QG, Mao GZ, Wang BD (2010) 1:250000 geological survey report of Nagqu county. China University of Geosciences Press, Tibet **(Chinese)**

Zeng M, Zhang X, Cao H, Ettensohn FR, Chen W, Lang X (2014) Late Triassic initial subduction of the Bangong-Nujiang Ocean beneath Qiangtang revealed: stratigraphic and geochronological evidence from Gaize, Tibet. Basin Res 1–11. https://doi.org/10.1111/bre.12105

Zhai QG, Jahn BM, Wang J, Su L, Mo XX, Wang KL, Tang SH, Lee HY (2013) The Carboniferous ophiolite in the middle of the Qiangtang terrane, Northern Tibet: SHRIMP U–Pb dating, geochemical and Sr–Nd–Hf isotopic characteristics. Lithos 168–169:186–199

Zhang YX (2007) Tectonic evolution of the middle–western Bangong–Nujiang suture, Tibet. A thesis submitted for the degree of doctorate at the Graduate School of The Chinese Academy of Sciences, 1–256 **(in Chinese with English abstract)**

Zhang KJ, Xia B, Zhang YX, Liu WL, Zeng L, Li JF, Xu LF (2014) Central Tibetan Meso–Tethyan oceanic plateau. Lithos 210–211:278–288

Zhang YX, Li ZW, Zhu LD, Zhang KJ, Yang WG, Jin X (2016) Newly discovered eclogites from the Bangong Meso-Tethyan suture zone (Gaize, central Tibet, western China): mineralogy, geochemistry, geochronology, and tectonic implications. Int Geol Rev 58:574–587

Zhao JH, Zhou MF (2007) Geochemistry of Neoproterozoic mafic intrusions in the Panzhihua district (Sichuan Province, SW China): implications for subduction–related metasomatism in the upper mantle. Precambrian Res 152:27–47

Zhao WJ, Liu K, Jiang ZT, Wu ZH, Zhao X, Shi DN, Xiong JY, Mechie J, Brown L, Hearn T, Guo JR, Haines SS (2004) Bangong Co–Nujiang suture zone, Tibet—a suggestion given by deep geophysical structure. Geol Bul China 23:623–635

Zhou MF, Malpas J, Robinson PT, Reynolds PH (1997) The dynamothermal aureole of the Donqiao ophiolite (northern Tibet). Can J Earth Sci 34:59–65

Zhu DC, Zhao ZD, Niu YL, Dilek Y, Hou ZQ, Mo XX (2013) The origin and pre-Cenozoic evolution of the Tibetan Platean. Gondwana Res 23:1429–1454